NASA TECHNICAL MEMORANDUM

NASA TM-73,247

(NASA-TM-73247) DETERMINING THE LIFT AND DRAG DISTRIBUTICNS ON A THREE-DIMENSIONAL AIRFOIL FROM FLOW-FIELD VELOCITY SURVEYS (NASA) 75 p HC A04/MF A01 CSCL 01A

N77-32079

Unclas
G3/02 47868

NASA TM-73,247

DETERMINING THE LIFT AND DRAG DISTRIBUTIONS ON A THREE-DIMENSIONAL AIRFOIL FROM FLOW-FIELD VELOCITY SURVEYS

Kenneth L. Orloff

Ames Research Center
Moffett Field, Calif. 94035

May 1977

NOMENCLATURE

AR	aspect ratio
C	refers to closed circuit around a wing section
CA	correction accuracy
C_D	total wing drag coefficient
C_L	total wing lift coefficient
D	total drag
D_p	pressure drag
D_{sf}	skin friction drag
F_y	spanwise force
$I(\ )$	integral operator
L	total lift
L_i	portion of circuit C, $i = 1, 2, 3, 4$
Re_c	Reynolds number based on wing chord
S	denotes control surface
S_i	portion of control surface S, $i = 1, \ldots, 6$
S_w	denotes wing surface
$T_\pm$	correction function
V	denotes control volume
V_∞	free-stream velocity
b	wing span
c	local wing chord
$\bar{c}$	mean geometric chord
c_d	section drag coefficient
c_ℓ	section lift coefficient

I, II MISSING

PRECEDING PAGE [redacted] NOT FILMED

$\vec{ds}, \vec{d\ell}$	infinitesimal length vectors for line integrations
$\vec{f}$	net body force
$\hat{n}$	outward unit normal to surface S
p	static pressure
p_0	total pressure at infinity
p_T	local total pressure
q_∞	free-stream dynamic pressure
t	time
$\vec{u}$	Eulerian fluid velocity
u_x	streamwise component of $\vec{u}$, positive downstream
u_y	spanwise component of $\vec{u}$
u_z	vertical component of $\vec{u}$, positive upward
x,y,z	Cartesian coordinates
$\hat{x},\hat{y},\hat{z}$	unit vectors along Cartesian directions x, y, z, respectively
y_0	spanwise location of trailing portion of a horseshoe vortex
γ	$\frac{cc_\ell}{8\pi}$
Γ	strength of vortex filament; circulation
$\vec{\zeta}$	vorticity
ζ_x,ζ_y,ζ_z	Cartesian components of $\vec{\zeta}$
μ	viscosity
ν	kinematic viscosity
ρ	fluid density
$\overleftrightarrow{\tau}$	shear stress tensor

Subscript e refers to an equivalent vortex

Superscript w denotes value in region of viscous wing wake

DETERMINING THE LIFT AND DRAG DISTRIBUTIONS ON A THREE-DIMENSIONAL AIRFOIL FROM FLOW-FIELD VELOCITY SURVEYS

Kenneth L. Orloff

Ames Research Center

SUMMARY

The application of the incompressible momentum integral equation to a three-dimensional airfoil is reviewed. The objective is to interpret the resulting equations in a way that suggests a reasonable experimental technique for determining the spanwise distributions of lift and drag. Consideration is given to constraints that must be placed on the character of the vortex wake structure shed by the wing, to provide the familiar relationship between lift and bound vorticity. It is shown that the induced drag distribution is not directly measurable, but can be obtained, via the lift distribution, approximately for a deflected wake and exactly for a planar wake. A novel technique is presented for obtaining the spanwise lift distribution from velocity surveys behind the wing. Moreover, it is shown that it is only necessary to survey a short distance above and below the wing trailing edge. While the measured lift coefficient is not the true value, it is, nevertheless, accurate. The necessary formalism is developed to correct these measured values by using an equivalent single vortex model to account for the unmeasured portion of the downward (or upward) momentum. Examples are presented for several typical loading distributions and the results of a numerical simulation of the suggested experiment are discussed.

INTRODUCTION

This paper deals with the application of the momentum integral equation to an airfoil that is generating both lift and drag. The objective is to interpret the resulting equations in a way that suggests a reasonable experimental technique for determining the spanwise distributions of lift and drag on a three-dimensional wing.

The motivation for the analysis has been largely due to the development and success of the laser velocimeter for conducting wind-tunnel flow diagnostics. Conventional velocity measuring techniques are either cumbersome or lack the required accuracy for conducting flow surveys. With the laser velocimeter, however, these drawbacks are overcome, and one may assume (as is done in the momentum analysis to follow) that accurate three-dimensional velocity data are available, as may be required in the application of the resulting equations.

The guiding philosophy in the analysis herein is that one should be dutifully aware of the true meaning of the data that are obtained experimentally. Flow characteristics that are easily measurable should be measured accurately; those that are not directly measurable with sufficient accuracy should be either replaced by equivalent measurements that are accurate or should be computed from an equivalent model of the flow, the parameters of which are based on the experimental data whose limitations are well understood.

MOMENTUM ANALYSIS

The integral form of the momentum equation may be written as

$$\int_V \frac{\partial}{\partial t}(\rho\vec{u})dV + \oint_S \rho\vec{u}(\vec{u}\cdot\hat{n})dS = \int_V \rho\vec{f}\,dV - \oint_S p\hat{n}\,dS + \oint_S (\hat{n}\cdot\vec{\tau})dS \qquad (1)$$

where $\vec{f}$ is the net body force per unit mass at points within the volume V, and $\vec{\tau}$ is the shear stress tensor at points on the closed surface S surrounding V. As is conventional, $\hat{n}$ is the outward unit normal to the surface S, p is the static pressure, ρ the fluid density, and $\vec{u}$ the Eulerian fluid velocity. If the flow is assumed to be steady, and no body forces are present, then equation (1) simplifies to

$$\oint_S \rho\vec{u}(\vec{u}\cdot\hat{n})dS = -\oint_S p\hat{n}\,dS + \oint_S (\hat{n}\cdot\vec{\tau})dS \qquad (2)$$

Two different control surfaces S are considered. Figure 1 depicts a control surface that would be used to compute the total lift and drag on the airfoil. The effects of the airfoil on the fluid are represented by corresponding variations in the velocities, static pressures, and shearing stresses on the control surface.

To compute the sectional lift and drag, the control surface in figure 2 is used. This surface is basically the same as that of figure 1, except for the infinitesimal thickness Δy. Also, while the wing surface S_W forms part of the closed surface S, the portions on S_5 and S_6 in figure 2 which cover the airfoil cross section are *not* part of the closed control surface.

For either of these control surfaces, the momentum equation (2) may be written as

$$-\int_{S_1} \rho\vec{u}u_x \, dy\, dz + \int_{S_2} \rho\vec{u}u_z \, dx\, dy + \int_{S_3} \rho\vec{u}u_x \, dy\, dz - \int_{S_4} \rho\vec{u}u_z \, dx\, dy$$

$$-\int_{S_5} \rho\vec{u}u_y \, dx\, dz + \int_{S_6} \rho\vec{u}u_y \, dx\, dz + \int_{S_w} \rho\vec{u}(\vec{u} \cdot \hat{n})dS$$

$$= -\int_{S_1} p\hat{n} \, dy\, dz - \int_{S_2} p\hat{n} \, dx\, dy - \int_{S_3} p\hat{n} \, dy\, dz - \int_{S_4} p\hat{n} \, dx\, dy - \int_{S_5} p\hat{n} \, dx\, dz$$

$$-\int_{S_6} p\hat{n} \, dx\, dz - \int_{S_w} p\hat{n} \, dS + \int_{S_1 \text{ thru } S_6} (\hat{n} \cdot \vec{t})dS + \int_{S_w} (\hat{n} \cdot \vec{t})dS \qquad (3)$$

We note the following four observations with respect to equation (3):

- $\int_{S_w} \rho\vec{u}(\vec{u} \cdot \hat{n})dS$ vanishes since $\vec{u} \cdot \hat{n} = 0$ at all points on the wing surface.
- Appendix A shows that $\int_{S_i} (\hat{n} \cdot \vec{\tau})dS = 0$ for $i = 1, \ldots, 6$ when the Reynolds number $(\bar{c}V_\infty/\nu) >> 1$.
- $\int_{S_w} (\hat{n} \cdot \vec{t})dS = -D_{sf}\hat{x}$ where D_{sf} is the drag due to skin friction. Also, we assume the lift generated by the shearing forces at the surface of the wing to be negligible compared to the pressure lift; hence, this integral has a negligible z-component.
- $-\int_{S_w} p\hat{n} \, dS$ represents the net pressure force exerted by the airfoil surface on the fluid. This is exactly minus the force exerted by the fluid on the airfoil. In component form,

$$-\int_{S_w} p\hat{n}_x \, dS = -D_p\hat{x} \quad \text{and} \quad -\int_{S_w} p\hat{n}_z \, dS = -L\hat{z}$$

  where both the form drag and the induced drag are contained in D_p.

Incorporating these observations into equation (3), we obtain, after separating into components,

$$\left.\begin{aligned}
L &= \int_{S_1} \rho u_x u_z \, dy\, dz - \int_{S_2} (\rho u_z^2 + p) dx\, dy - \int_{S_3} \rho u_x u_z \, dy\, dz \\
&\quad + \int_{S_4} (\rho u_z^2 + p) dx\, dy + \int_{S_5} \rho u_y u_z \, dx\, dz - \int_{S_6} \rho u_y u_z \, dx\, dz \\
D &= D_{sf} + D_p = \int_{S_1} (\rho u_x^2 + p) dy\, dz - \int_{S_2} \rho u_x u_z \, dx\, dy - \int_{S_3} (\rho u_x^2 + p) dy\, dz \\
&\quad + \int_{S_4} \rho u_x u_z \, dx\, dy + \int_{S_5} \rho u_x u_y \, dx\, dz - \int_{S_6} \rho u_x u_y \, dx\, dz \\
F_y &= \int_{S_1} \rho u_x u_y \, dy\, dz - \int_{S_2} \rho u_y u_z \, dx\, dy - \int_{S_3} \rho u_x u_y \, dy\, dz \\
&\quad + \int_{S_4} \rho u_y u_z \, dx\, dy + \int_{S_5} (\rho u_y^2 + p) dx\, dz - \int_{S_6} (\rho u_y^2 + p) dx\, dz
\end{aligned}\right\} \quad (4)$$

F_y, a spanwise force, can exist for the control surface of figure 2, but vanishes for a wing having bilateral symmetry with a control surface as shown in figure 1.

Several of the terms in equations (4) require a knowledge of the static pressure on the control surface. Experimentally, these pressures would be difficult to measure accurately; undetected, small changes over a large surface area can produce a considerable error in the resulting force computation. Since the accurate measurement of the velocity is somewhat more convenient (especially with the laser velocimeter), the static pressures in equations (4) are replaced with the total pressure and the local velocity

$$p = p_T - \frac{\rho}{2} (u_x^2 + u_y^2 + u_z^2)$$

This substitution is helpful in two ways: (1) a difficult measurement has been replaced by simpler ones; (2) the total pressure p_T is the total head p_0 in all regions that have not suffered viscous losses.

Using this replacement of the static pressure and nondimensionalizing the velocities by V_∞ and x, y, and z by $\bar{c}$, the mean geometric chord, we obtain

$$
\left.
\begin{aligned}
\frac{L}{q_\infty} &= 2\int_{S_1} u_x u_z \, dy\, dz - \int_{S_2} (u_z{}^2 - u_x{}^2 - u_y{}^2) dx\, dy - 2\int_{S_3} u_x u_z \, dy\, dz \\
&\quad + \int_{S_4} (u_z{}^2 - u_x{}^2 - u_y{}^2) dx\, dy + 2\int_{S_5} u_y u_z \, dx\, dz - 2\int_{S_6} u_y u_z \, dx\, dz \\
\frac{D}{q_\infty} &= \int_{S_1} (u_x{}^2 - u_y{}^2 - u_z{}^2) dy\, dz - 2\int_{S_2} u_x u_z \, dx\, dy \\
&\quad - \int_{S_3} (u_x{}^2 - u_y{}^2 - u_z{}^2) dy\, dz + 2\int_{S_4} u_x u_z \, dx\, dy + 2\int_{S_5} u_x u_y \, dx\, dz \\
&\quad - 2\int_{S_6} u_x u_y \, dx\, dz + \int_{S_3} \left(\frac{p_\infty - p_T}{q_\infty}\right) dy\, dz \\
\frac{F_y}{q_\infty} &= 2\int_{S_1} u_x u_y \, dy\, dz - 2\int_{S_2} u_y u_z \, dx\, dy - 2\int_{S_3} u_x u_y \, dy\, dz + 2\int_{S_4} u_y u_z \, dx\, dy \\
&\quad + \int_{S_5} (u_y{}^2 - u_x{}^2 - u_z{}^2) dx\, dz - \int_{S_6} (u_y{}^2 - u_x{}^2 - u_z{}^2) dx\, dz
\end{aligned}
\right\} \quad (5)
$$

where p_0 is the total pressure at infinity and p_T is the local total pressure at any point on S_3.

Total Lift and Drag

We now proceed to let all surfaces of the control volume in figure 1 expand to infinity, with the exception of surface S_3. To maintain $F_y = 0$, S_5 and S_6 expand symmetrically about the centerline of the wing. On these remotely located surfaces, $u_y \approx u_z \approx 0$ and $u_x \approx 1$. If we substitute into equations (5) the coefficient representations for lift and drag, $L = q_\infty C_L(b\bar{c})$ and $D = q_\infty C_D(b\bar{c})$,

$$
\left.
\begin{aligned}
C_L &= \frac{2}{\mathit{AR}}\int_{-\infty}^{\infty}\int_{-\infty}^{\infty} u_x u_z \, dy\, dz \\
C_D &= \frac{1}{\mathit{AR}}\int_{-\infty}^{\infty}\int_{-\infty}^{\infty} \left(1 - u_x{}^2 + u_y{}^2 + u_z{}^2 + \frac{p_0 - p_T}{q_\infty}\right) dy\, dz
\end{aligned}
\right\} \quad (6)
$$

where the integration is over the rear surface S_3.

In equations (6), the analytical expressions for the lift and drag coefficients require a knowledge of the velocity and total pressure distributions in the wake of the airfoil only. On the other hand, it is unlikely that the implied technique would be implemented experimentally, since the region of the wake that must be measured is extensive; further, the procedure would be influenced by the interference of the wind-tunnel walls. Even if the entire flow could be mapped accurately, the same values could be obtained with much less difficulty by using a force balance. Of greater interest are the wing sectional properties, which cannot be obtained from force measurements.

Section Lift and Drag

We return to equations (5) and consider the control surface presented in figure 2. The differential dy is now Δy and the area integrations over S_1, S_2, S_3, and S_4 become line integrations along L_1, L_2, L_3 and L_4, respectively, with width Δy. L and D are represented by $L = q_\infty c_\ell (c\Delta y)$, and $D = q_\infty c_d (c\Delta y)$, where the coefficients, c_ℓ and c_d, are now the section values and c is the local chord. Equations (5) are now written as

$$\left.\begin{aligned}
cc_\ell &= 2\int_{L_1} u_x u_z \, dz - \int_{L_2} (u_z^2 - u_x^2 - u_y^2) dx - 2\int_{L_3} u_x u_z \, dz \\
&\quad + \int_{L_4} (u_z^2 - u_x^2 - u_y^2) dx + \frac{2}{\Delta y}\left[\int_{S_5} u_y u_z \, dx \, dz - \int_{S_6} u_y u_z \, dx \, dz\right] \\
cc_d &= \int_{L_1} (u_x^2 - u_y^2 - u_z^2) dz - 2\int_{L_2} u_x u_z \, dx - \int_{L_3} (u_x^2 - u_y^2 - u_z^2) \, dz \\
&\quad + 2\int_{L_4} u_x u_z \, dx + \frac{2}{\Delta y}\left[\int_{S_5} u_x u_y \, dx \, dz - \int_{S_6} u_x u_y \, dx \, dz\right] \\
&\quad + \int_{L_3} \left(\frac{p_0 - p_T}{q_\infty}\right) dz
\end{aligned}\right\} \quad (7)$$

The equation for the spanwise force, F_y, has been dropped from the analysis at this point because it is found not to lead to anything of special interest for configurations that have bilateral symmetry.

The assumption is now made that the flow velocity around the airfoil is changing smoothly and slowly enough with respect to y that the integrands in the remaining surfaces integrals in equations (7) can be expressed to first order as

$$\left.\begin{aligned}
(u_y u_z)_6 &= (u_y u_z)_5 + \left[\frac{\partial}{\partial y} (u_y u_z)\right]_S \Delta y \\
(u_x u_y)_6 &= (u_x u_y)_5 + \left[\frac{\partial}{\partial y} (u_x u_y)\right]_S \Delta y
\end{aligned}\right\} \quad (8)$$

where subscripts 5 and 6 refer to the surfaces S_5 and S_6, respectively, and the subscript S indicates evaluation of the derivative at the surface spanned by the closed circuit C, defined by L_1, L_2, L_3, and L_4. The normal to S is taken in the positive y-direction. Substituting equations (8) into the surface integrations of equations (7),

$$\left.\begin{aligned}
\frac{2}{\Delta y}\left(\int_{S_5} u_y u_z \, dx\, dz - \int_{S_6} u_y u_z \, dx\, dz\right) &= -2\int_S \frac{\partial}{\partial y}(u_y u_z) dx\, dz \\
\frac{2}{\Delta y}\left(\int_{S_5} u_x u_y \, dx\, dz - \int_{S_6} u_x u_y \, dx\, dz\right) &= -2\int_S \frac{\partial}{\partial y}(u_x u_y) dx\, dz
\end{aligned}\right\} \quad (9)$$

Appendix B shows that the surface integrals on the righthand side of equations (9) can be written as

$$\left.\begin{aligned}
-2\int_S \frac{\partial}{\partial y}(u_y u_z) dx\, dz = {} & -2\int_{L_1} u_x u_z \, dz + \int_{L_2} (u_z^2 - u_x^2 - u_y^2) dx \\
& + 2\int_{L_3} u_x u_z \, dz - \int_{L_4} (u_z^2 - u_x^2 - u_y^2) dx \\
& + 2\iint_S u_x \left(\frac{\partial u_x}{\partial z} - \frac{\partial u_z}{\partial x}\right) dx\, dz - 2\iint_S u_y \left(\frac{\partial u_z}{\partial y} - \frac{\partial u_y}{\partial z}\right) dx\, dz \\
-2\int_S \frac{\partial}{\partial y}(u_y u_z) dx\, dz = {} & -\int_{L_1} (u_x^2 - u_y^2 - u_z^2) dz + 2\int_{L_2} u_x u_z \, dx \\
& + \int_{L_3} (u_x^2 - u_y^2 - u_z^2) dz - 2\int_{L_4} u_x u_z \, dx \\
& + 2\iint_S u_y \left(\frac{\partial u_y}{\partial x} - \frac{\partial u_x}{\partial y}\right) dx\, dz - 2\iint_S u_z \left(\frac{\partial u_x}{\partial z} - \frac{\partial u_z}{\partial x}\right) dx\, dz
\end{aligned}\right\} \quad (10)$$

Equations (7) may, therefore, be reduced using equations (10)

$$\left.\begin{aligned}
cc_\ell &= 2\iint_S (u_x \zeta_y - u_y \zeta_x) dx\, dz \\
cc_d &= 2\iint_S (u_y \zeta_z - u_z \zeta_y) dx\, dz + \int_{L_3} \left(\frac{p_0 - p_T}{q_\infty}\right) dz
\end{aligned}\right\} (11)$$

where $\vec{\zeta}$ = curl $\vec{u}$ is the vorticity vector.

Equations (11) are not yet in a form to suggest a reasonable experimental technique for determining the aerodynamic coefficients c_ℓ and c_d. The method implied by these equations requires detailed distributions of the velocity field over the entire surface S. The additional need for the vorticity distributions requires that the derivatives of the velocity be determined from the data, reducing the accuracy of coefficient results. Hence, before our analysis can continue, some assumptions must be made regarding the character of the flow, in order to further simplifty equations (11).

Lifting-Line Approximation

If the flow field of interest can be adequately described by a lifting-line model, at least over the region enclosed by the closed circuit C, then equations (11) can be simplified considerably. The assumed geometry, shown in figure 3, reduces the wing cross-sectional area to zero about the bound vortex. The surface denoted by the double integration in equations (11) is therefore the entire area spanned by C. This allows the use of Stoke's Theorem, which reduces the problem to a line integral around C, if equations (11) can be put into a form that is compatible with this theorem.

To apply Stoke's Theorem, we note two implicit restrictions of the lifting-line model:

- If the lines of shed vorticity are allowed downward deflection, due to mutual induction, but spanwise deflection is forbidden, then ζ_y is nonzero only along the bound vortex. Hence, it is only nonzero at $x = z = 0$, where we must have $u_x = 1$.

- ζ_x vanishes along the bound vortex. It is nonzero only along a trailing line of shed vorticity of strength $d\Gamma(y)$. However, if no spanwise wake deflection is allowed, then $U_y = 0$ along these lines.

Using the two restrictions above, the lift coefficient is

$$cc_\ell = 2\iint_S (u_x\zeta_y - u_y\zeta_x)dx\,dz = 2\iint_S \zeta_y\,dx\,dz$$

Writing $\zeta_y = \hat{y} \cdot \text{curl}\,\vec{u}$ we may apply Stoke's Theorem,

$$cc_\ell = 2\iint_S \hat{y} \cdot \text{curl}\,\vec{u}\,dx\,dz = 2\oint_C \vec{u} \cdot d\vec{\ell} \tag{12}$$

where $\hat{y}$ is precisely the unit normal to the surface S. This is a familiar result for two-dimensional flows, but it is also valid for a three-dimensional flow with the two lifting-line restrictions above.

If the lifting-line model is used to simplify the drag coefficient, the "planar wake" assumption must be made, which additionally requires $\zeta_z = 0$, whereas this value was not restricted for the lift coefficient. With this additional restriction,

$$cc_d = -2\iint_S u_z\zeta_y\,dx\,dz + \int_{L_3}\left(\frac{p_0 - p_T}{q_\infty}\right)dz$$

Since ζ_y is nonzero only at $x = z = 0$ on S, then

$$cc_d = -u_z\left(2\iint_S \zeta_y\,dx\,dz\right) + \int_{L_3}\left(\frac{p_0 - p_T}{q_\infty}\right)dz$$

where u_z is the value of the downwash at the bound vortex at the point where it is intersected by S. This is further reduced to

$$cc_d = -u_z(cc_\ell) + \int_{L_3} \left(\frac{p_0 - p_T}{q_\infty}\right) dz \tag{13}$$

The first term in equation (13) is precisely the induced drag. However, it is not possible to measure experimentally the induced downwash u_z at the chordwise location of the wing center of pressure (bound vortex). Hence, from lifting-line theory we replace u_z with (in dimensional form),

$$u_z(y) = \frac{1}{4\pi} \int_{-b/2}^{b/2} \frac{\frac{\partial\Gamma(y')}{\partial y'}}{y - y'} \, dy' \tag{14}$$

Writing $\Gamma(y') = (1/2)V_\infty c(y')c_\ell(y')$, the nondimensional form of equation (14) becomes

$$u_z(y) = \frac{1}{8\pi} \int_{-b/2\bar{c}}^{b/2\bar{c}} \frac{\partial/\partial y'(cc_\ell)}{y - y'} \, dy' \tag{15}$$

Substituting equation (15) into equation (13),

$$cc_d = \frac{cc_\ell}{8\pi} \int_{-b/2\bar{c}}^{b/2\bar{c}} \frac{\partial/\partial y'(cc_\ell)}{y - y'} \, dy' + \int_{L_3} \frac{p_0 - p_T}{q_\infty} \, dz \tag{16}$$

Hence, the induced drag is not explicitly determined, but is only implicit via the lift distribution under severe restrictions (i.e., no vertical or spanwise wake deflection). At any rate, it is first necessary to determine the lift distribution accurately from equation (12).

EXPERIMENTAL CONSIDERATIONS

If the lifting-line model is assumed to represent the real flow adequately, at least in the region of the control surface, then equation (2) suggests that one can determine the section-lift coefficient experimentally by measuring the appropriate velocity components on the closed contour C. If the orientation of the loop remains rectilinear to the flow, then the extent of circuit C is not restricted as long as the vorticity passing through it remains constant. As the loop expands, however, the velocity variation about free-stream conditions becomes smaller; to sense these changes with sufficient accuracy to perform the integration in equation (12) becomes increasingly difficult.

To measure the flow velocities along the loop C with a laser velocimeter, one must have "spanwise" optical access to the flow, as indicated in figure 4. Such a view of the selected spanwise location may, however, be hindered by obstacles such as engine nacelles, flap pods, etc. To measure around these obstacles, the loop may become so large that the accuracy of the measurement is compromised. Additionally, spanwise access may not be feasible, as in a large wind tunnel (e.g., Ames 40- by 80-Foot Wind Tunnel). See figure 5. Hence, it would be convenient to extend the results of the previous sections to the spanwise loading when only limited optical access is available. The next section presents such an extension of the theory.

Lift Distribution from Wake Surveys

Equation (12) can be written

$$cc_\ell = 2\oint_C \vec{u}\cdot d\vec{\ell} = 2\left[\int_{L_1} u_z\,dz + \int_{L_2} u_x\,dx - \int_{L_3} u_z\,dz - \int_{L_4} u_x\,dx\right]$$

If the boundaries L_1, L_2, and L_4 are allowed to expand to infinity, then $u_z = 0$ on L_1 and $u_x = 1$ on L_2 and L_4. Then we have

$$cc_\ell = -2\int_{L_3} u_z\,dz = -2\int_{-\infty}^{\infty} u_z\,dz \qquad (17)$$

Because an experimental traverse along L_3 can be made over only a finite distance between z_1 and z_2 (see fig. 6), we express equation (17) as

$$cc_\ell = -2\int_{z_2}^{\infty} u_z\,dz - 2\int_{-\infty}^{z_1} u_z\,dz + (cc_\ell)_{meas} \qquad (18)$$

where

$$(cc_\ell)_{meas} = -2\int_{z_1}^{z_2} u_z\,dz$$

is the "measured" value between the limits z_1 and z_2.[1] The first and second terms in equation (18) relate to the z-component of the linear momentum, which is present outside the measured region. This momentum must be accounted for if we are to have an accurate value for the section lift coefficient.

The difference to be expected between the true value of cc_ℓ and the measured value $(cc_\ell)_{meas}$ can be shown by formulating a computer code to

[1] Because the experiment is simulated precisely on a minicomputer, the numerical computation of the lift coefficient is referred to as the "measured" value; the quotation marks are intended to distinguish this from an actual wind-tunnel measurement.

generate a flow field and then performing the experiment numerically. Appendix C presents the details of this flow-field generation routine and the relevant equations. Note that the generator allows for a nonplanar wake, but there is no spanwise vorticity, ζ_y, in the free wake. Figure 7 shows, in flow chart form, the experimental simulation that uses this velocity field as a basis for the "measurements." This routine is carried out on a high-speed minicomputer with a graphics display terminal. The figures shown in Appendix D are reproductions of the hardcopy from this terminal.

Figure 8 compares the known cc_ℓ distribution with that determined by a wake survey over a finite distance, z_1 to z_2. The points for the "measured" loading have been obtained from the experimental simulation routine. The flow-field generator produces a superposition of two horseshoe systems, one shed inboard at $y = 1.32$ and the other near the tip at $y = 3.38$. The core radius of the outer vortex, set to 0.12, provides $cc_\ell = 0$ at the wing tip, $y = 3.50$. The survey limits have been chosen as one mean geometric chord $\bar{c}$ both above and below the "trailing edge"; the survey is made at 0.9 mean chord behind the bound vortex. The comparison is understandably poor because a significant portion of downward momentum is contained in the unmeasured region and has been neglected. Also, note that the "measured" loading in figure 8 does not extend inboard from $y = 0.5$. This has been done intentionally since it is unlikely that one could obtain data any closer in a real experiment because of fuselage width.

Correction of "Measured" Lift Distribution Using Equivalent Vortex Model

The difference between the "actual" and "measured" loadings in figure 8 can be accounted for by modeling the flow analytically in the unmeasured regions. The parameters of the model are determined by the character of the data obtained in the measured region. The correction terms in equation (18) can then be computed and the corrected lift coefficient determined.

The assumption is made that there exists a single "equivalent" horseshoe vortex that contains an amount of downward momentum in the unmeasured regions that is very nearly equal to the momentum generated in these regions by the span loading of interest. If it is further assumed that this horseshoe is planar, then the induced velocity component u_z at any point (x, y, z) in the flow due to the equivalent system can be shown to be (see appendix C),

$$u_{z_e} = -\gamma_e\left[Ax + B\left(y_{0_e} - y\right) + C\left(y_{0_e} + y\right)\right] \tag{19}$$

where the subscript e refers to the equivalent vortex, $\gamma_e = (cc_\ell)_e/8\pi$ is the strength of the vortex, y_{0_e} is the spanwise location of the trailing portion of the horseshoe, and A, B, and C are given by

$$A = \left[\frac{y_+}{\sqrt{x^2 + y_+^2 + z^2}} + \frac{y_-}{\sqrt{x^2 + y_-^2 + z^2}}\right](x^2 + z^2)^{-1}$$

$$B = \left[\frac{x}{\sqrt{x^2 + y_-^2 + z^2}} + 1\right](y_-^2 + z^2)^{-1}$$

$$C = \left[\frac{x}{\sqrt{x^2 + y_+^2 + z^2}} + 1\right](y_+^2 + z^2)^{-1}$$

where $y_+ = y_{0_e} + y$ and $y_- = y_{0_e} - y$.

Substituting equation (19) into equation (18),

$$cc_\ell = 2\gamma_e[xI(A) + y_-I(B) + y_+I(C)] + (cc_\ell)_{meas} \tag{20}$$

where $I(F)$ is the definite integral operator

$$I(F) = \int_{z_2}^{\infty} F\,dz + \int_{-\infty}^{z_1} F\,dz \tag{21}$$

The indefinite form of the integrals in equation (21) may be evaluated and shown to be

$$\left.\begin{aligned}
\int A\,dz &= \frac{1}{x}\left[\tan^{-1}\left(\frac{y_+ \sin\theta}{x}\right) + \tan^{-1}\left(\frac{y_- \sin\phi}{x}\right)\right] \\
\int B\,dz &= \frac{1}{y_-}\left[\tan^{-1}\left(\frac{x \sin\phi}{y_-}\right) + \tan^{-1}\left(\frac{z}{y_-}\right)\right] \\
\int C\,dz &= \frac{1}{y_+}\left[\tan^{-1}\left(\frac{x \sin\theta}{y_+}\right) + \tan^{-1}\left(\frac{z}{y_+}\right)\right]
\end{aligned}\right\} \tag{22}$$

where

$$\sin\theta = \frac{z}{\sqrt{x^2 + y_+^2 + z^2}} \quad \text{and} \quad \sin\phi = \frac{z}{\sqrt{x^2 + y_-^2 + z^2}}$$

With attention being given to the signs of the numerators and denominators in equation (22), equation (20) can be expressed as

$$
\left.
\begin{aligned}
cc_\ell &= -\frac{1}{2\pi}(cc_\ell)_e T_+ + (cc_\ell)_{meas} && \text{for} \quad -y_{0_e} \le y \le y_{0_e} \\
cc_\ell &= -\frac{1}{2\pi}(cc_\ell)_e T_- + (cc_\ell)_{meas} && \text{for} \quad y > y_{0_e} \\
cc_\ell &= \frac{1}{2\pi}(cc_\ell)_e T_- + (cc_\ell)_{meas} && \text{for} \quad y < -y_{0_e}
\end{aligned}
\right\} \quad (23)
$$

where

$$
T_\pm = \tan^{-1}\left(\frac{y_+ \sin\theta_2}{x}\right) + \tan^{-1}\left(\frac{x \sin\theta_2}{y_+}\right) \pm \tan^{-1}\left(\frac{y_- \sin\phi_2}{x}\right)
$$

$$
\pm \tan^{-1}\left(\frac{x \sin\phi_2}{y_-}\right) + \tan^{-1}\left(\frac{z_2}{y_+}\right) \pm \tan^{-1}\left(\frac{z_2}{y_-}\right) - \pi \mp \pi \quad (24)
$$

This solution is restricted to $z_2 = -z_1$; subscript 2 in equation (24) denotes evaluation of $\sin\theta$ and $\sin\phi$ at $z = z_2$. The distance behind the bound vortex at which the survey has been made is given by x, and y is the spanwise location where the correction is desired.

Note, from equations (23) and (24), that the correction is completely determined by specifying two values: $(cc_\ell)_e$ and y_{0_e}, the strength and location, respectively, of the equivalent vortex. To obtain these values, two known conditions are invoked relevant to the corrected distribution cc_ℓ. These two conditions are:

- The value of cc_ℓ at the wing tip must be zero.
- The area beneath the cc_ℓ distribution must equal the total lift coefficient of the wing, C_L.

The first condition is satisfied only if y_{0_e} is located inboard of the wing tip. It then follows from the second equation of equations (23) that

$$
(cc_\ell)_e = \frac{2\pi}{T_-}(cc_\ell)_{meas\ at\ tip} \quad (25)
$$

T_- contains both y_{0_e} and $(cc_\ell)_e$ so that closure of the solution requires the second condition to be invoked. This is accomplished numerically by iterating the solution, as indicated in figure 9.

Results from Numerical Experiments

Figure 10 shows the results obtained by applying this iteration scheme (fig. 9) to the data in figure 8. The equivalent vortex is located at $y_{0_e} = 2.79$, with a strength $(cc_\ell)_e = 1.42$. The area beneath the corrected data matches $C_L = 1.08$ to within 1%.

The agreement between the corrected data and the "actual" loading in figure 10 is good, except in the areas noted. If, however, the extent of the measured region were greater than $z_2 = 1.0$, in this case, then the correction scheme should be more accurate. To verify this, we refer to figure 11, which shows uncorrected loadings for several survey distances z_2 from 0.5 to 2.0 chords above and below the wing. Clearly, as survey distance z_2 increases, more momentum contributes to the "measured" value. Figure 12 presents the corrected loadings for the most extreme values of z_2 in figure 11. As expected, the loading is more faithfully reproduced at $z_2 = 2.0$ than at $z_2 = 0.5$.

To quantify the accuracy with which this correction scheme reproduces the "actual" loading, the area mismatch in figure 10 is used and the following definition is applied:

$$\text{Correction accuracy} = \left(1 - \frac{\text{area mismatch}}{C_L}\right) \times 100\% \qquad (26)$$

The correction accuracy (abbreviated CA) in figure 12 indicates a mismatch of less than 4% for the survey of 2.0 chords, compared to more than 20% mismatch for a survey of 0.5 chords.

It is of interest to consider the application of this equivalent vortex correction technique to several different loading distributions. The loadings chosen to represent typical aircraft configurations are described in table 1. The results obtained for wake surveys of these loadings at $x = 0.9$ for $z_2 = 0.5$ and $z_2 = 2.0$ are presented in figures 13, 14, and 15. Intermediate values of z_2 and a complete accounting of the results are provided in appendix D.

Figure 15 indicates that, for the elliptic distribution, a correction accuracy of 95.8% can be attained for a wake survey of only 0.5 chords above and below the wing. This finding is in sharp contrast to the value of 78.1% obtained for the flap/tip combination (fig. 12) with the same survey distance. Moreover, the 30°/0° and 30°/30° loadings indicate correction accuracies that are intermediate between these values. To understand this trend more thoroughly, we refer to figure 16, which shows the correction accuracy for the loadings studied as a function of survey distance z_2. These data suggest that as the loading distribution deviates further from the elliptic, the required survey distance must increase to maintain a given percentage accuracy in the agreement with the "actual" distribution. Equivalently, this means that the single vortex equivalent model becomes less adequate as the loading shifts predominantly inboard, exhibiting less resemblance to an elliptic loading. On the other hand, appendix D reveals that an acceptable reproduction of the loading is obtained with the single vortex correction when the correction accuracy is greater than about 93%. Therefore, if one were to conduct the wind-tunnel experiment with a laser velocimeter, a minimum survey distance would be required to obtain an accurate (93%) loading distribution. Figure 16 suggests the following guidelines for any loading similar to those presented herein:

Loading	Minimum survey distance (93% accuracy)
Flap/tip	1.4
30/0	1.0
30/30	0.8
Elliptic	0.3

Distribution of Induced Drag

Equation (16) provides a means for determining the spanwise distribution of induced drag:

$$(cc_d)_i = \frac{cc_\ell}{8\pi}\int_{-b/2\bar{c}}^{b/2\bar{c}} \frac{\partial/\partial y'(cc_\ell)}{y - y'}\,dy' \tag{27}$$

This expression was obtained by assuming that: (1) the wake is entirely planar ($\zeta_y = \zeta_z = 0$), and (2) the induced drag can be expressed as the product $-u_z(cc_\ell)$ with u_z obtained from the lift distribution. Even though the flows in the previous section have induced downward deflection, it is instructive to assume that the "actual" induced drag can be represented by $-u_z(cc_\ell)$, and that the computed drag can be obtained numerically from equation (27) using the cc_ℓ data resulting from the wake surveys of the previous section.

Figures 17, 18, and 19 present the induced drag distributions obtained from the loadings in figures D-9, D-14, and D-20 of appendix D, for the 30/0, 30/30, and elliptic cases, respectively. As the loading shifts predominantly inboard (30/0 and 30/30), the high induced drag at the tip decreases, as expected. These figures must, however, only be used to infer regions of high and low induced drag and overall trends, since equation (27) contains assumptions that cannot be closely satisfied. Even the "actual" drag shown is not precise because the wake is not truly planar, and $-u_z$ is obtained from the known (deflected) flowfield. Nevertheless, the three examples in these figures have been included for completeness.

Conveniently, the velocity wake surveys may be conducted along the same path L_3 as that used to determine the viscous drag. Knowledge of the three-dimensional velocity along this line allows one to preset the orientation of the total pressure probe so as to align it more precisely with the mean flow direction, thereby improving its accuracy.

SUMMARY AND LIMITATIONS

An analysis of the momentum integral equation has shown that the local section-lift coefficient on a wing is determined solely by the net vorticity passing through a closed circuit C when certain restrictions are placed on the character of the inviscid wake structure. It was shown that, when downward deflection of the shed vorticity is present, but spanwise deflection is absent within the circuit C, the relationship in equation (12) is valid.

The analysis has assumed the bound vortex line to lie along the y-axis with $\zeta_x = 0$. The analysis does, however, proceed identically from equation (11) when wing sweep is considered. In this case, ζ_x has a finite value along the bound vortex, but spanwise deflection of the trailing vortex system is again forbidden, and symmetry provides $u_y = 0$ at all points on the bound vortex. Hence, the examples presented for the swept-wing transport-type loadings are still meaningful.

A method has been developed for determining the spanwise lift distribution from wake measurements only. The equivalent vortex correction technique has been shown to be adequate as long as the wake survey line extends sufficiently far above and below the wing trailing edge. The required survey distance has been shown to be governed by the degree to which the loading is concentrated inboard.

TABLE 1.- LOADINGS USED FOR FLOW-FIELD SIMULATION

Loading designation	Number of horseshoe vortices used for flow-field generator	C_L	Remarks
Flap/tip	2	1.08	Loading presented in figures 8, 10, 11, and 12. Both vortices of same sense.
30°/0°	3	1.12	Similar to flap/tip loading but with additional vortex of opposite sense shed from inboard edge of the flap. Simulates transport aircraft of aspect ratio 7 with inboard flap deflected by 30° and the outboard flap retracted.
30°/30°	5	1.19	Simulates transport aircraft of aspect ratio 7 with both flaps deflected by 30°.
Elliptic	8	1.66	Approximates, stepwise, an elliptic lift distribution.

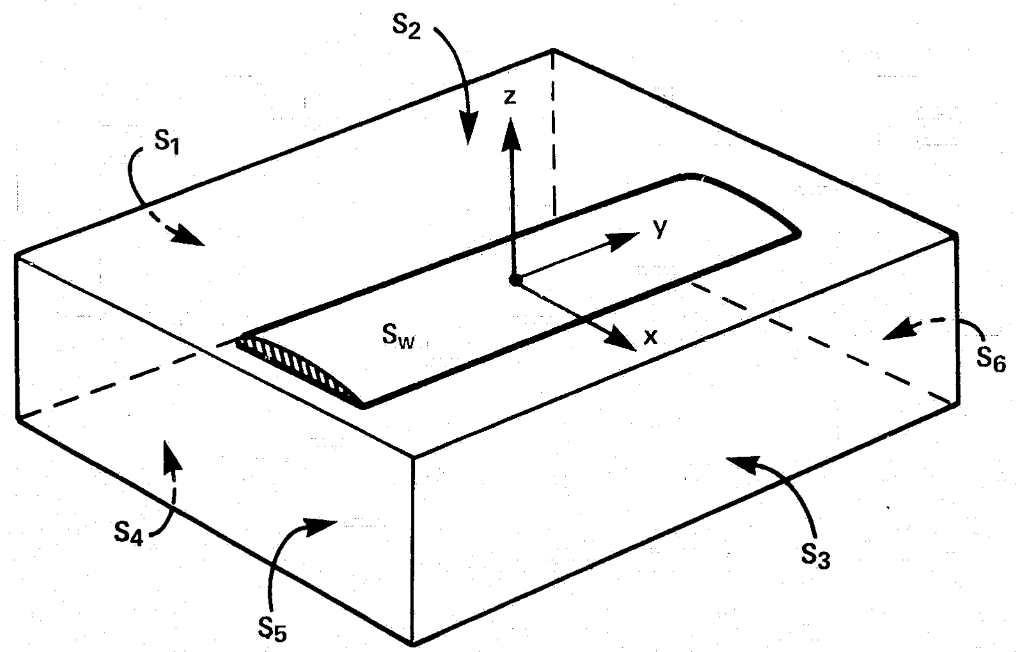

Figure 1.- Control surface for computation of total lift and drag.

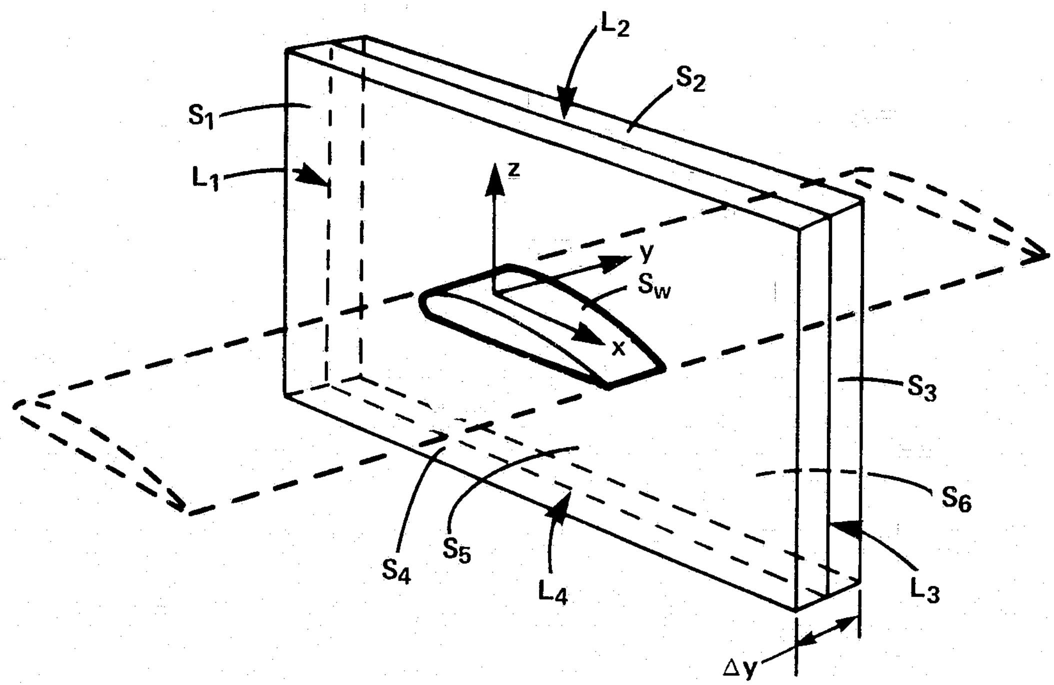

Figure 2.- Control surface for computation of section lift and drag.

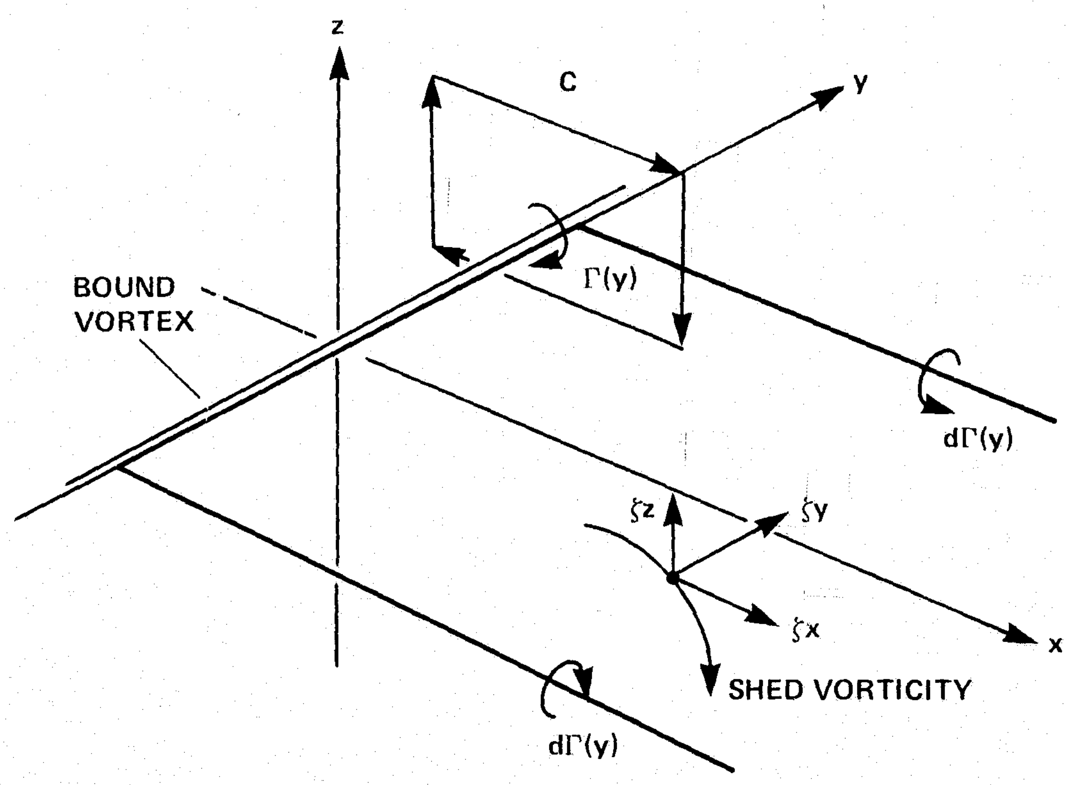

Figure 3.- Lifting line approximation showing integration circuit C, bound and shed vorticity.

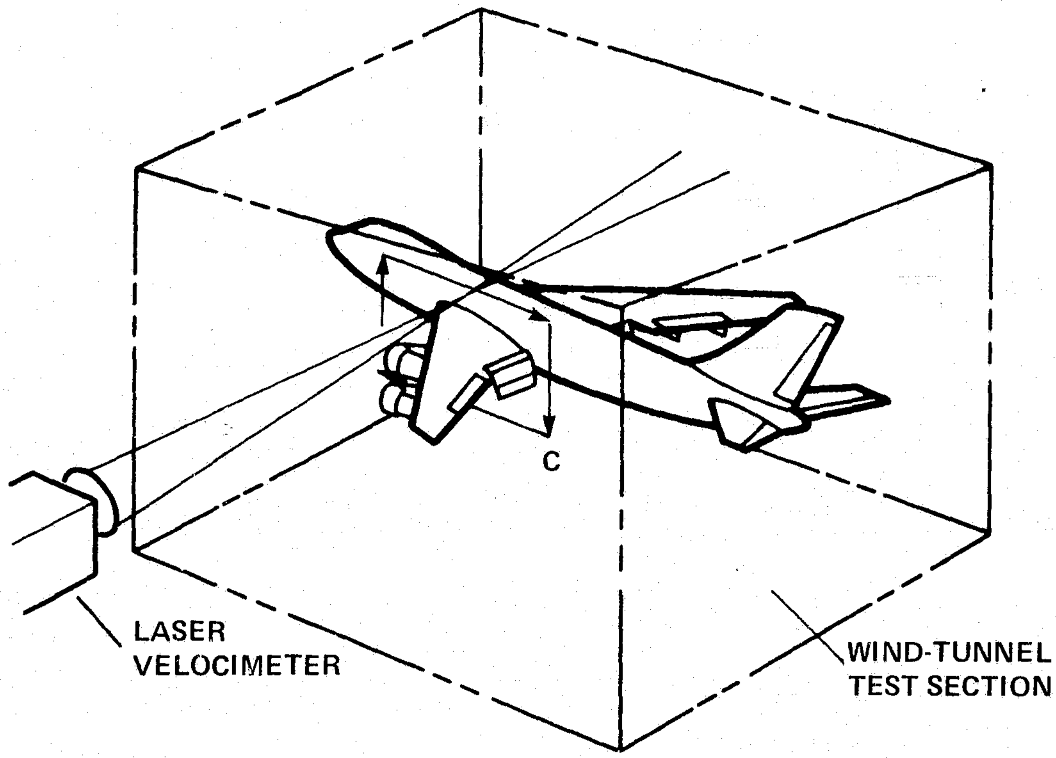

Figure 4.- Experimental situation which allows for spanwise optical access. Typical of smaller facilities (e.g., Ames 7- by 10-Foot Wind Tunnel). Section lift coefficient can be determined from $cc_\ell = 2\oint_C \vec{u} \cdot d\vec{\ell}$.

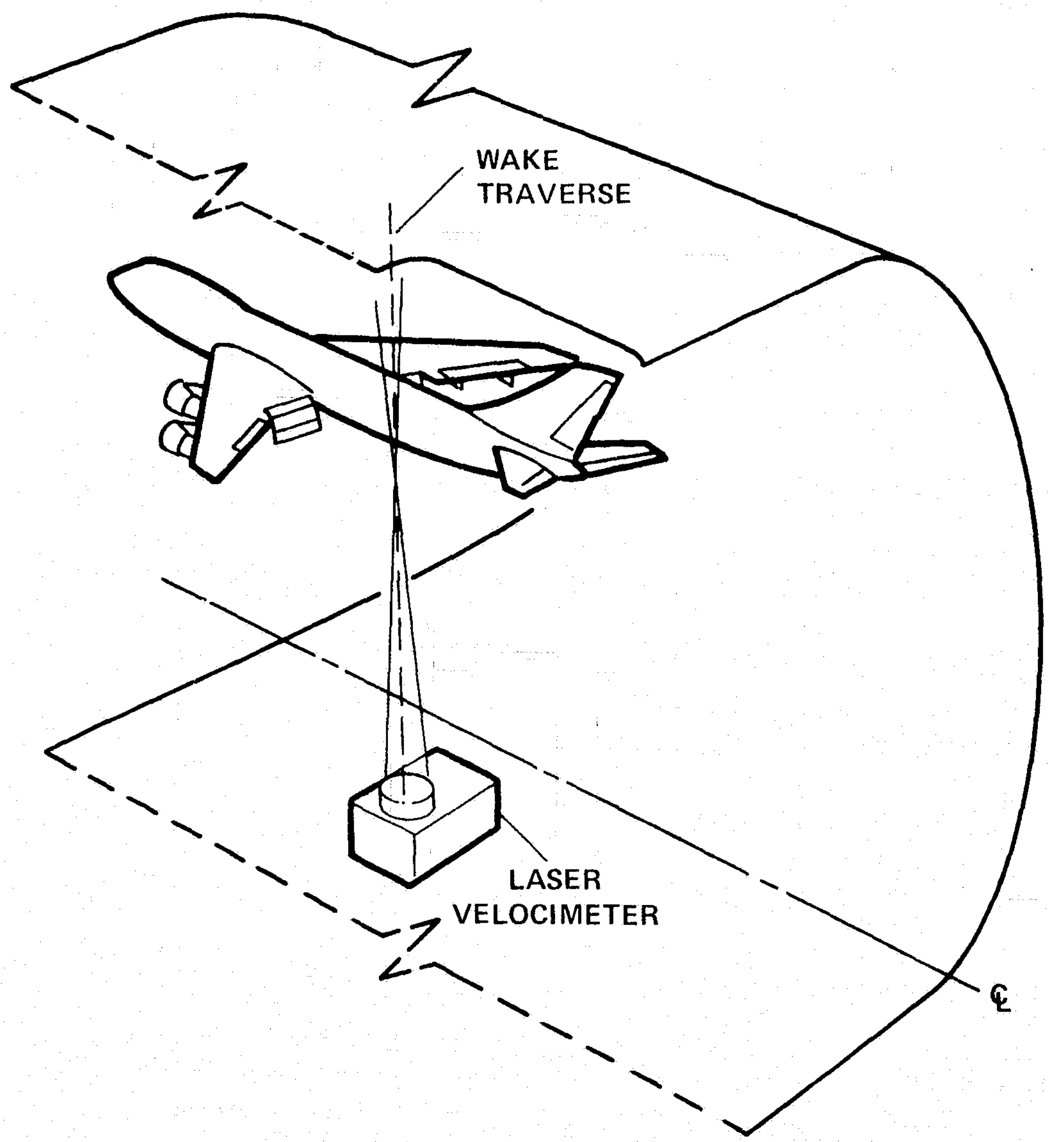

Figure 5.- Experimental situation which only allows for limited optical access. Typical of large facility (Ames 40- by 80-Foot Wind Tunnel). Section lift coefficient determined by correcting measured cc_ℓ using an equivalent vortex.

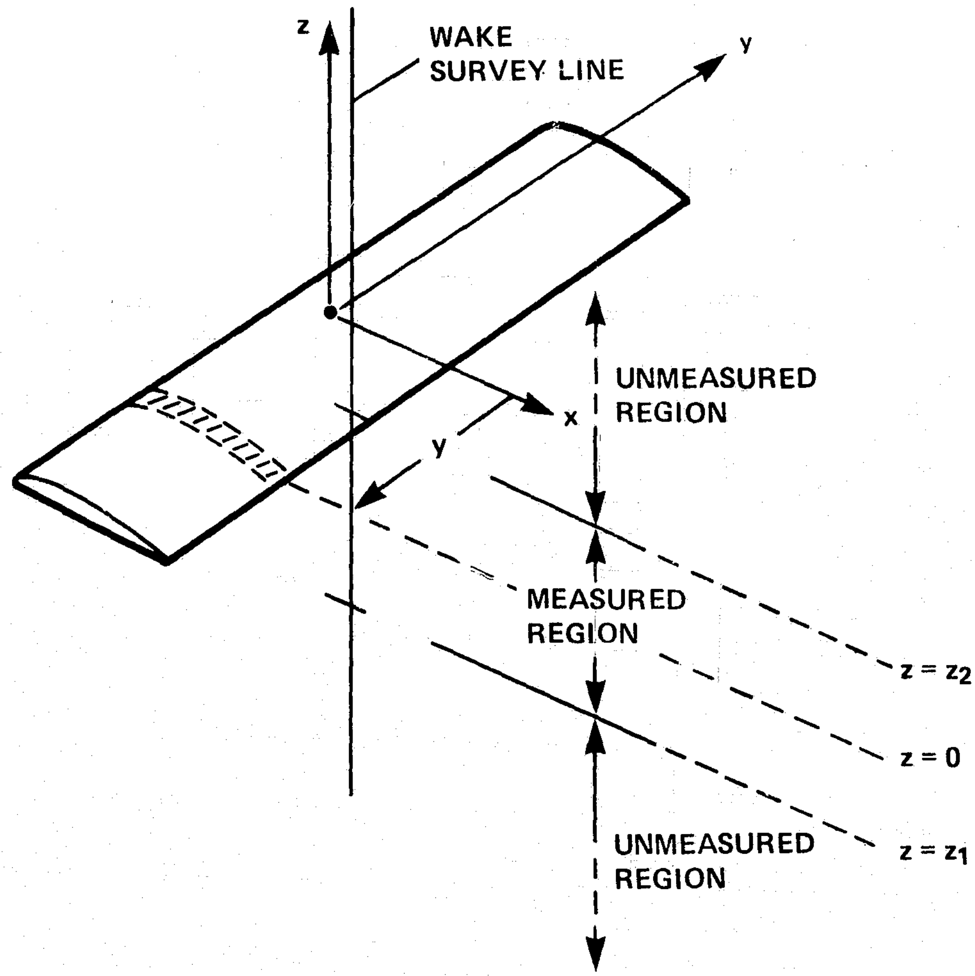

Figure 6.- Measured region determined by finite length of experimental traverse over only portion of wake survey line. Flow is modeled in unmeasured regions to generate a correction to measured value of cc_{ℓ}.

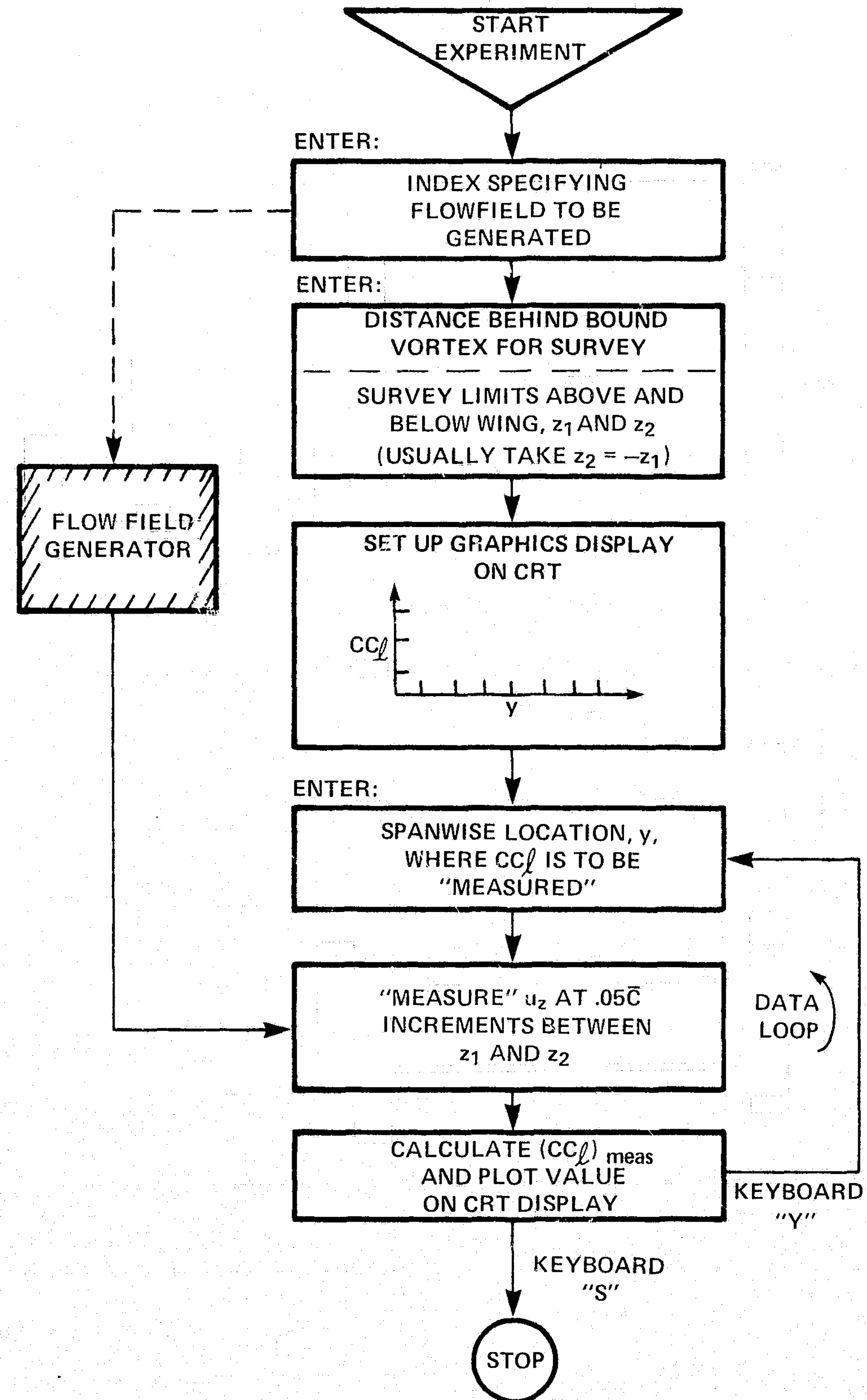

Figure 7.- Flow chart for numerical wake survey experiment.

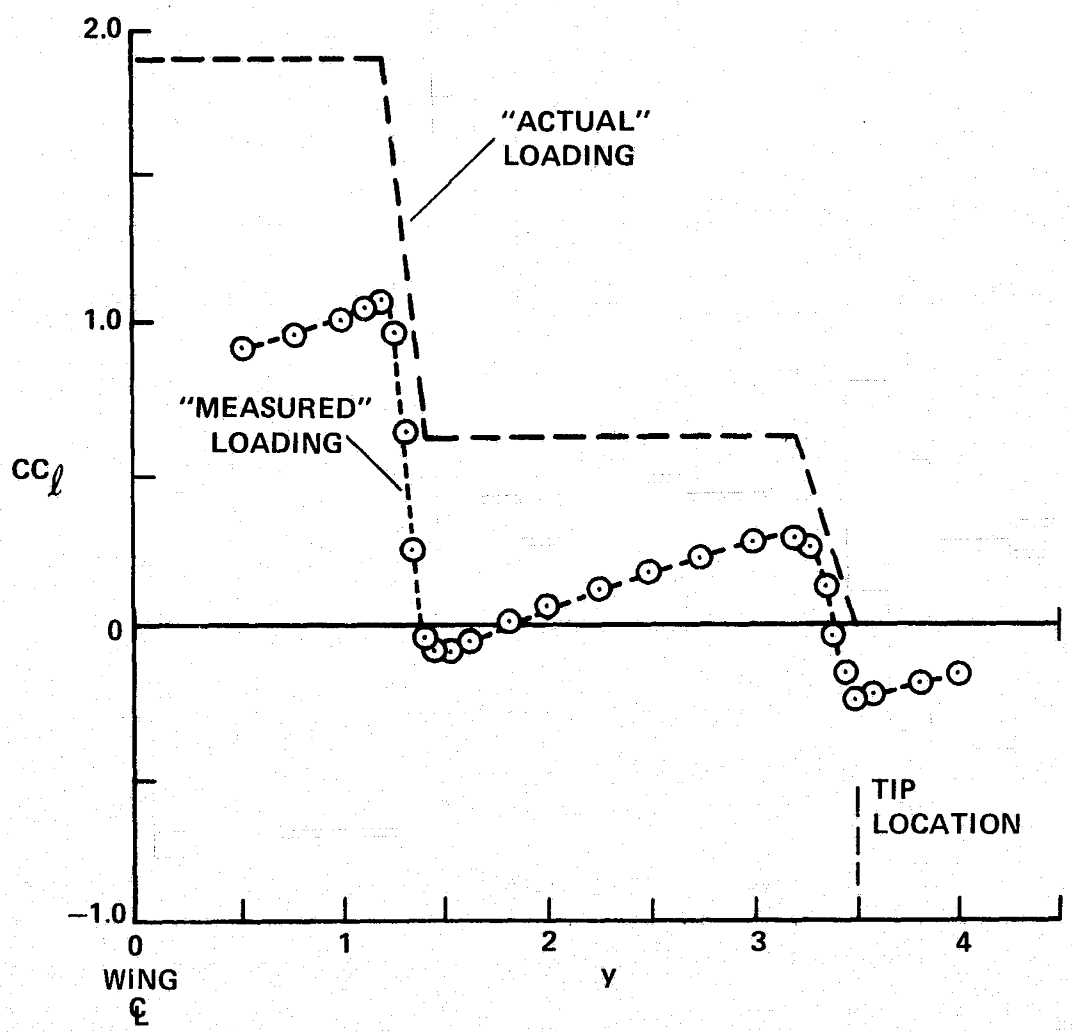

Figure 8.- Difference between "actual" and "measured" loading distribution for finite traverse distance. $z_2 = -z_1 = 1.0$, $x = 0.9$.

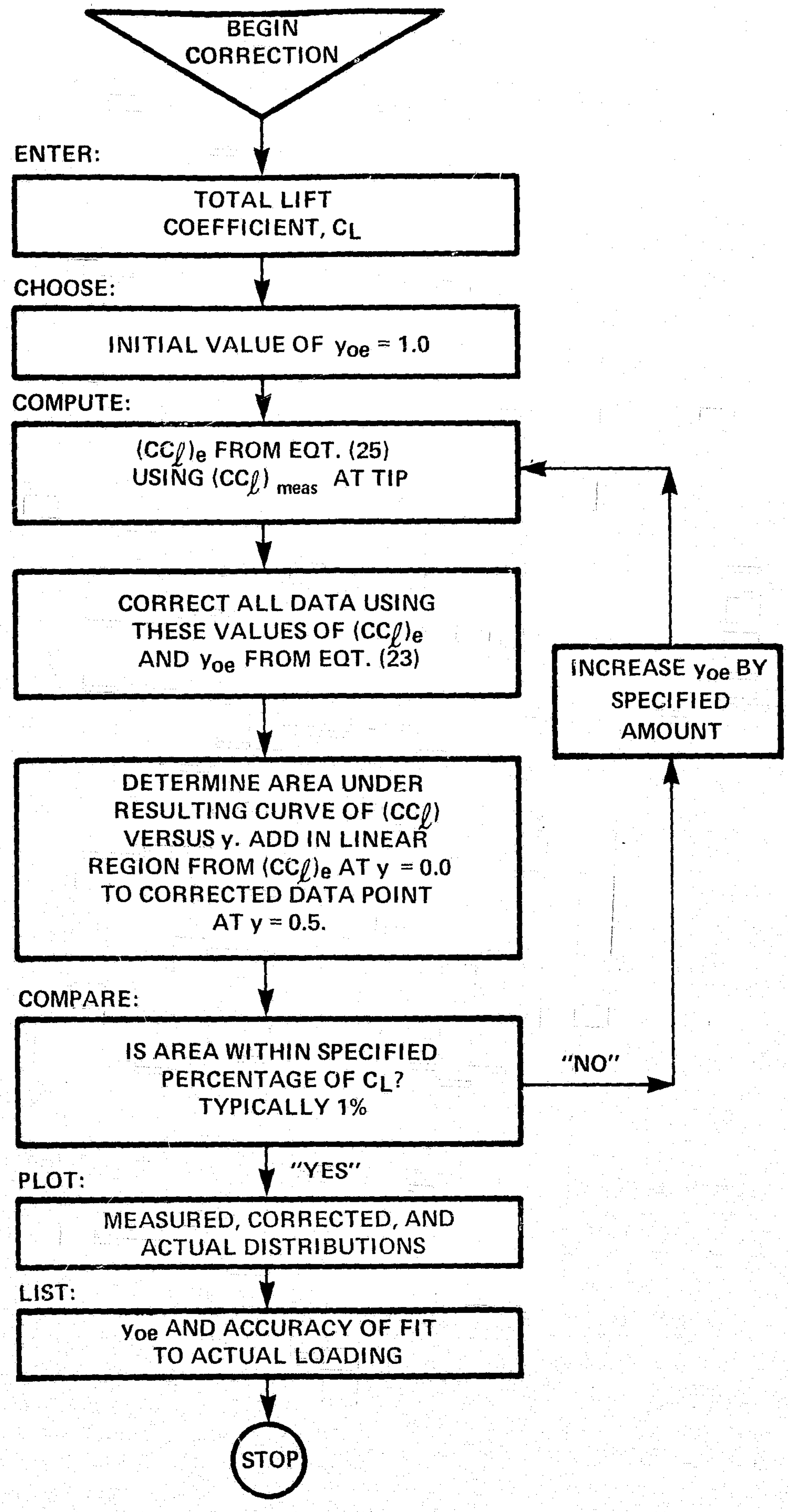

Figure 9.- Flow chart for numerical correction to lift coefficient.

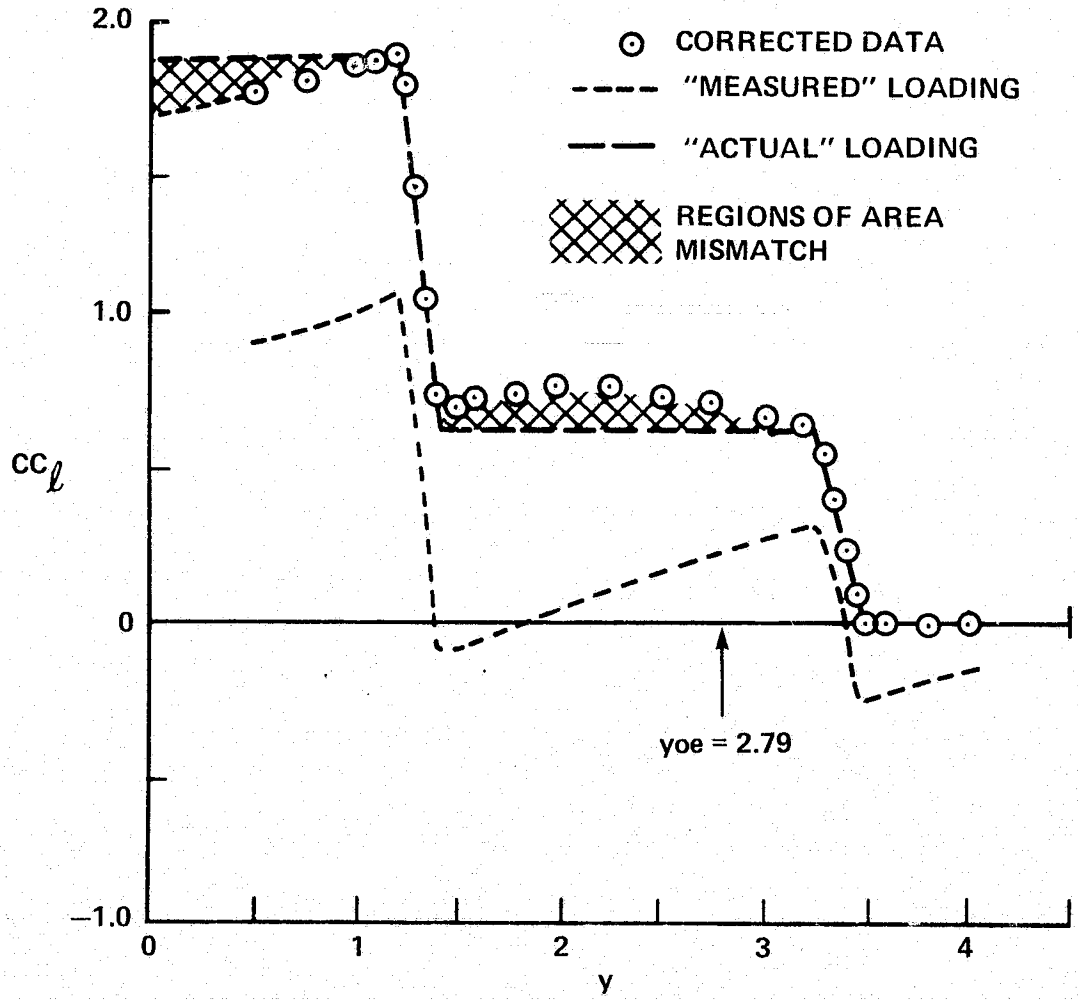

Figure 10.- Corrected data showing comparison to "actual" loading when lift coefficient $C_L = 1.08$ is matched to within 1%. Equivalent vortex has strength of $(cc_{\ell})_e = 1.42$.

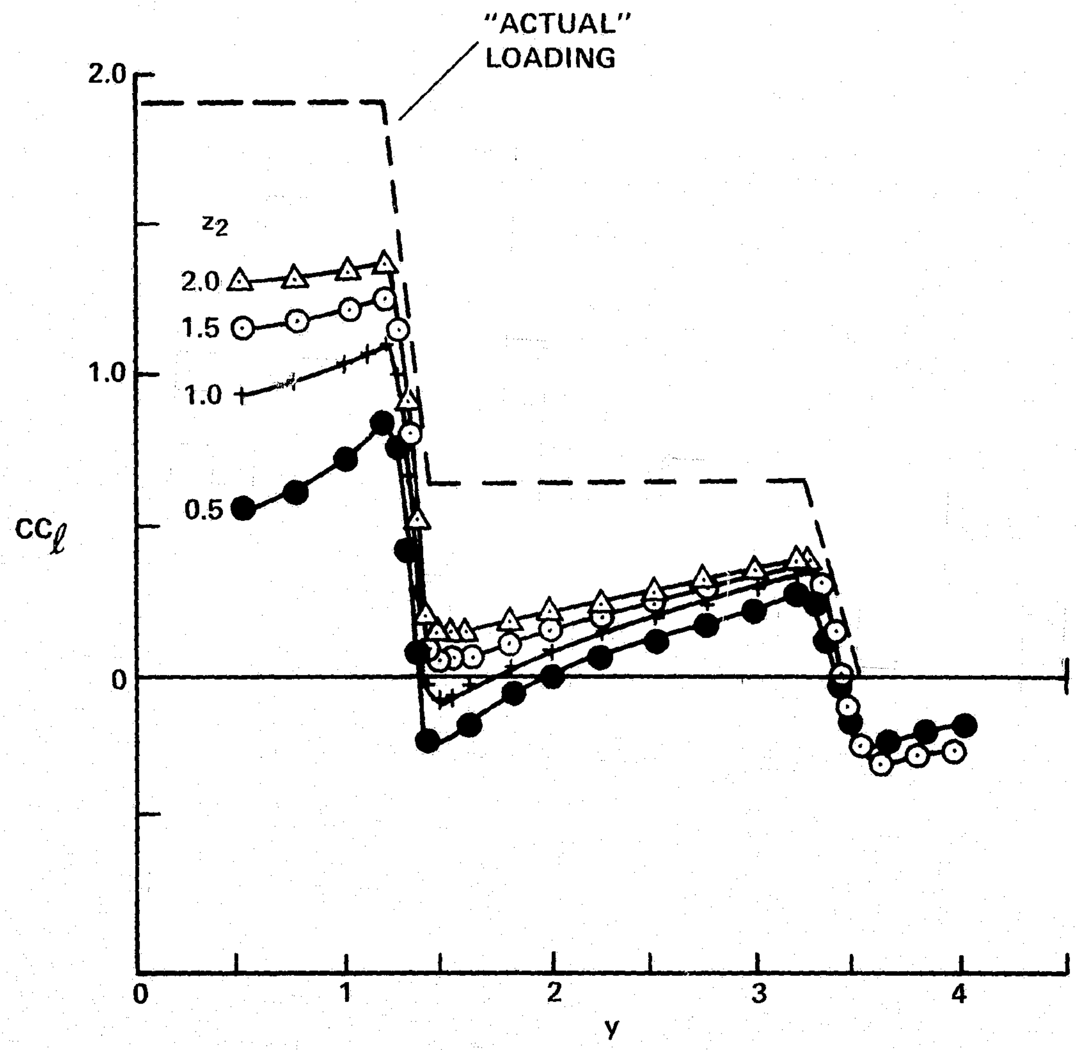

Figure 11.- Uncorrected loading for several survey distances.

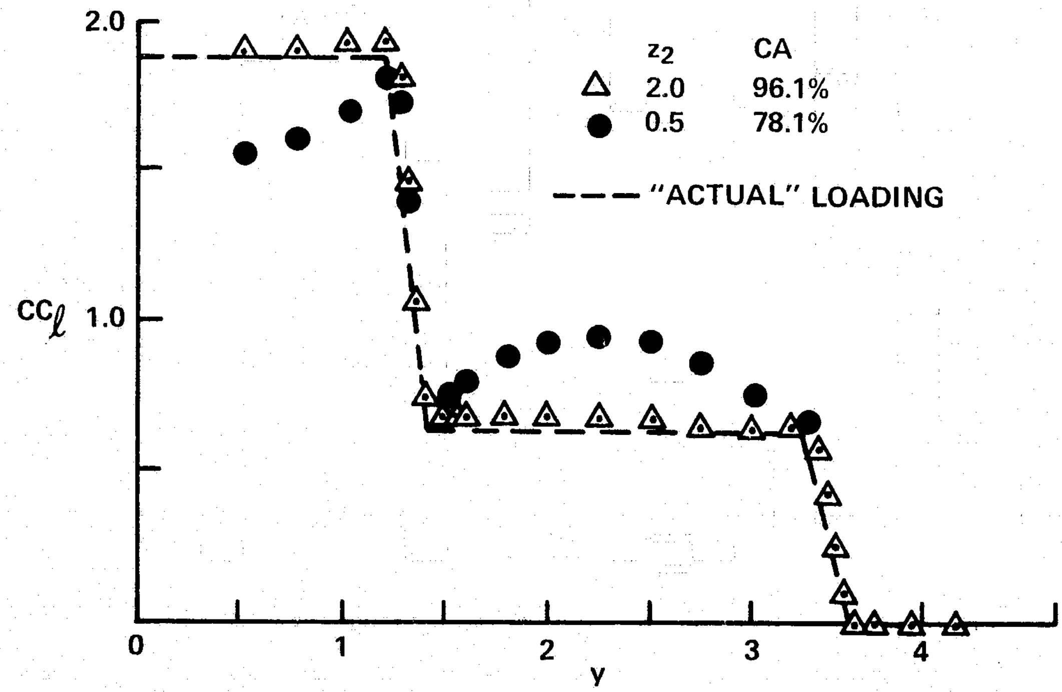

Figure 12.- Corrected loadings showing the increased accuracy of the correction with increasing survey distance.

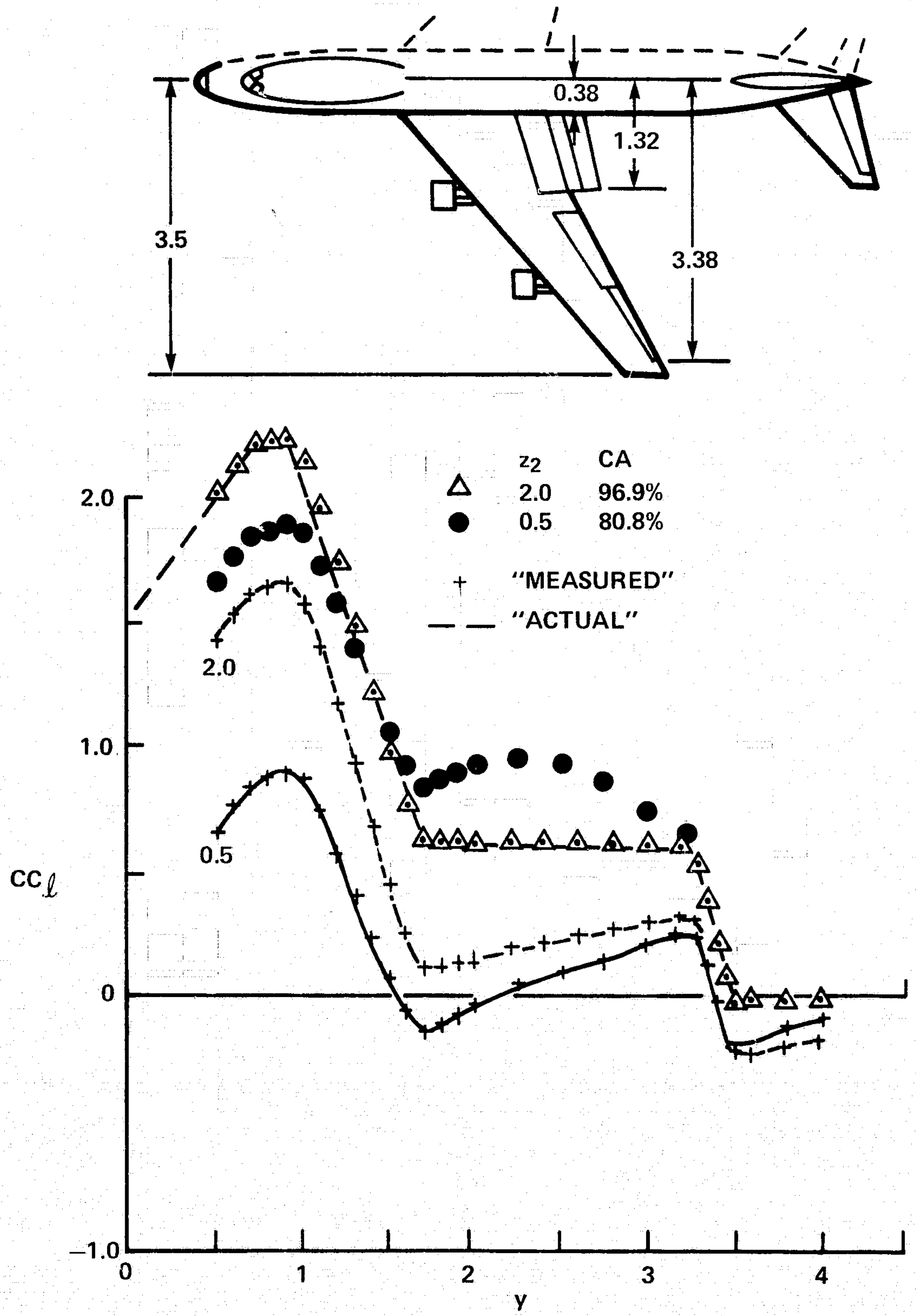

Figure 13.- Equivalent vortex correction applied to 30°/0° loading. Drawing shows assumed locations of shed vortices for flow-field generator.

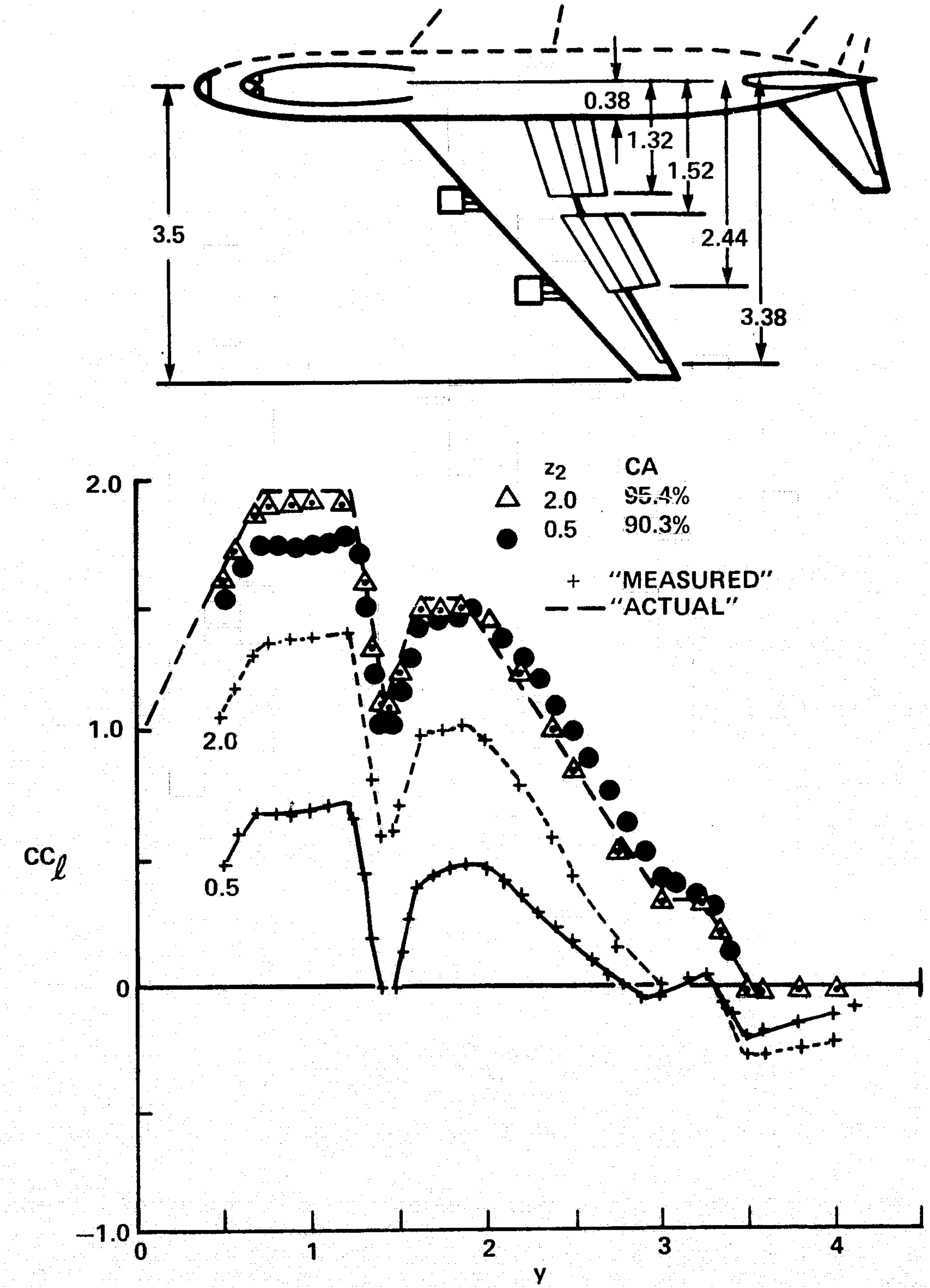

Figure 14.- Equivalent vortex correction applied to 30°/30° loading. Drawing shows assumed locations of shed vortices for flow-field generator.

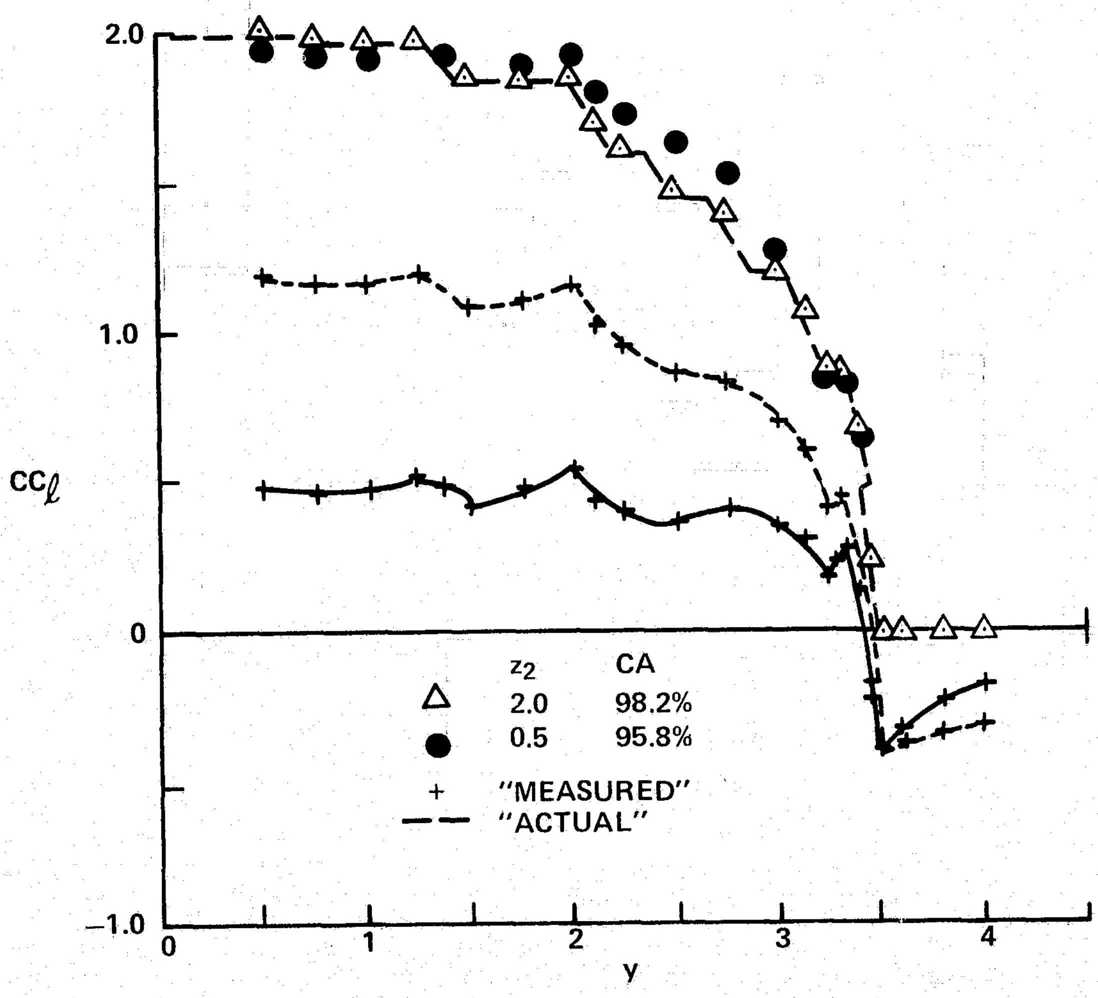

Figure 15.- Equivalent vortex correction applied to an approximately elliptic loading.

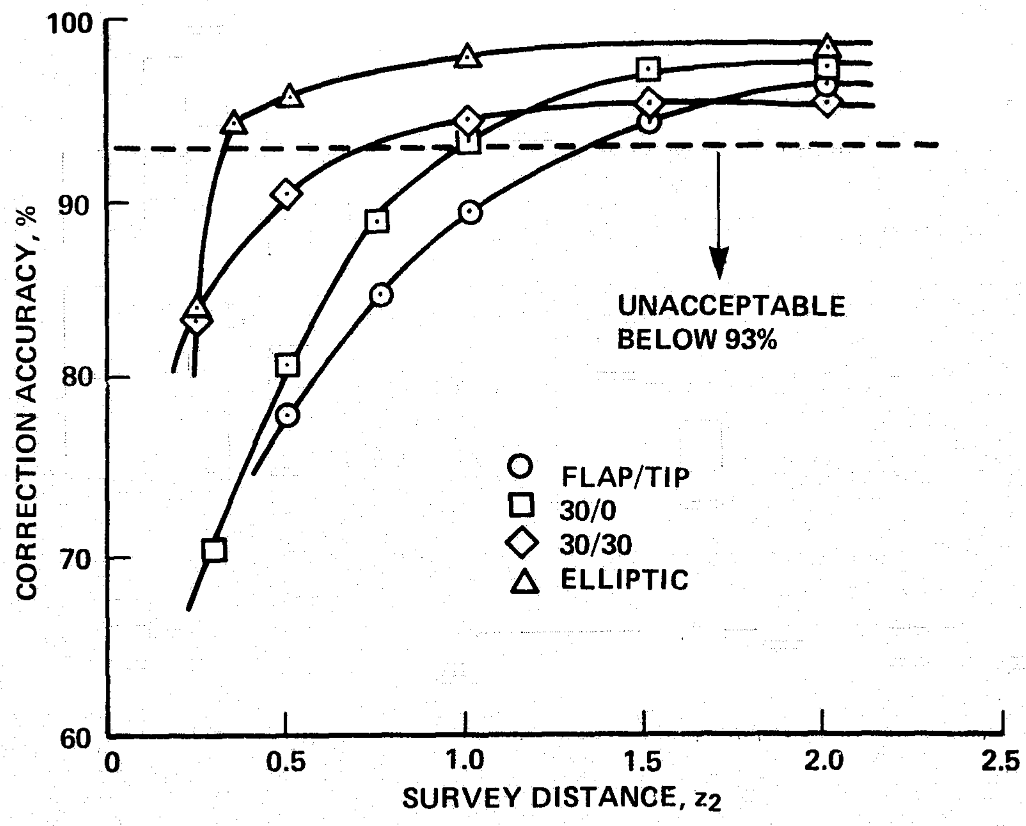

Figure 16.- Correction accuracy of the equivalent vortex model as a function of survey distance for several loadings.

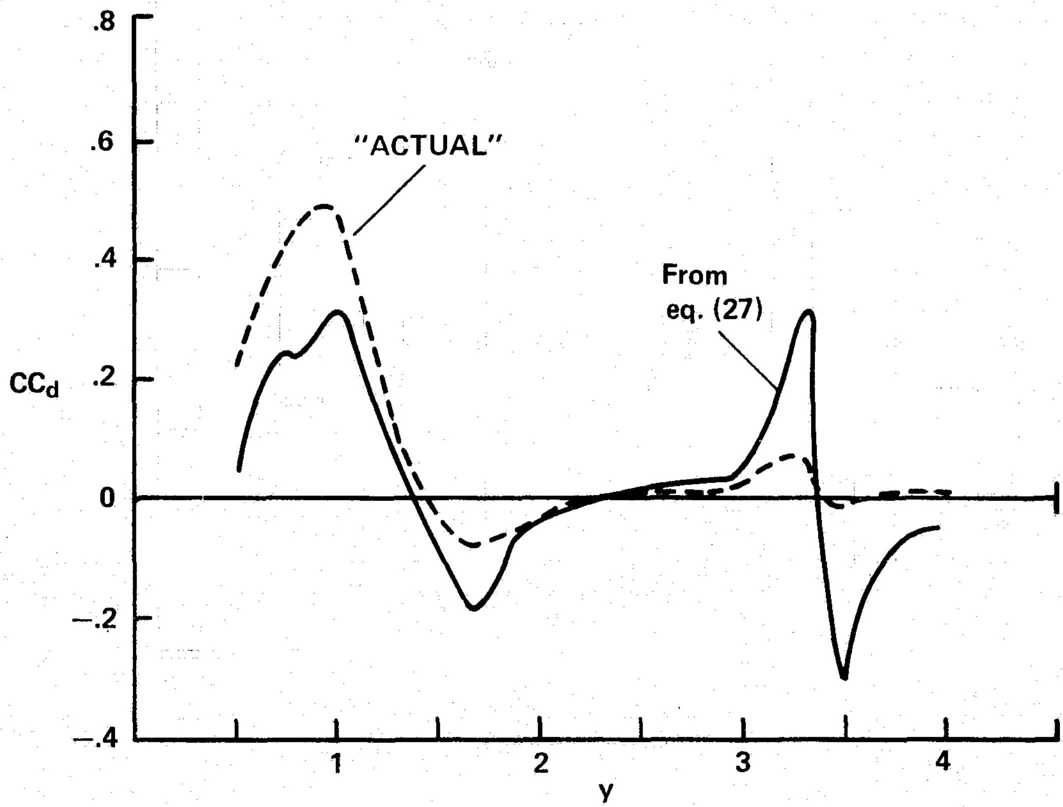

Figure 17.- Comparison of "actual" induced drag, $-u_z(cc_\ell)_{meas}$, and the distribution computed from equation (27). 30°/0° loading. C_L = 1.12.

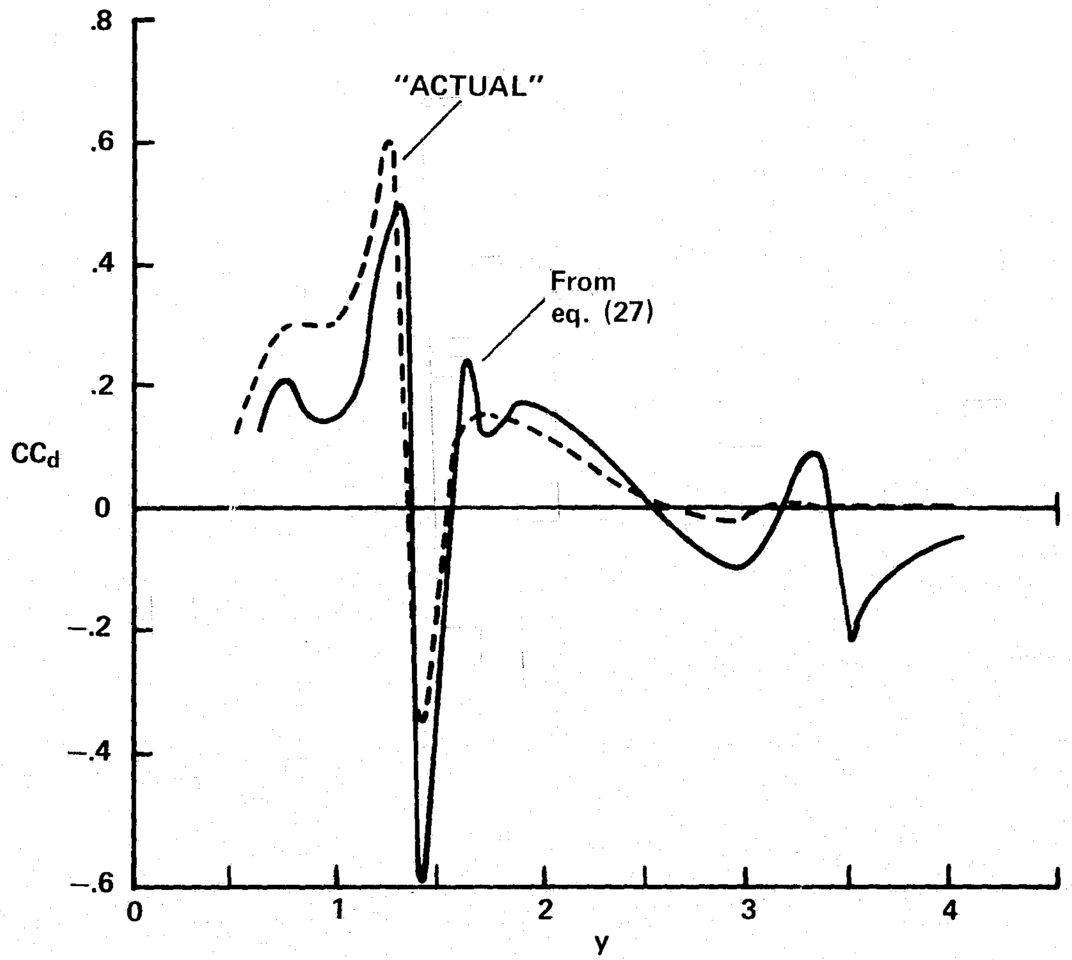

Figure 18.- Comparison of "actual" induced drag, $-u_z(cc_\ell)_{meas}$, and the distribution computed from equation (27). 30°/30° loading. C_L = 1.19.

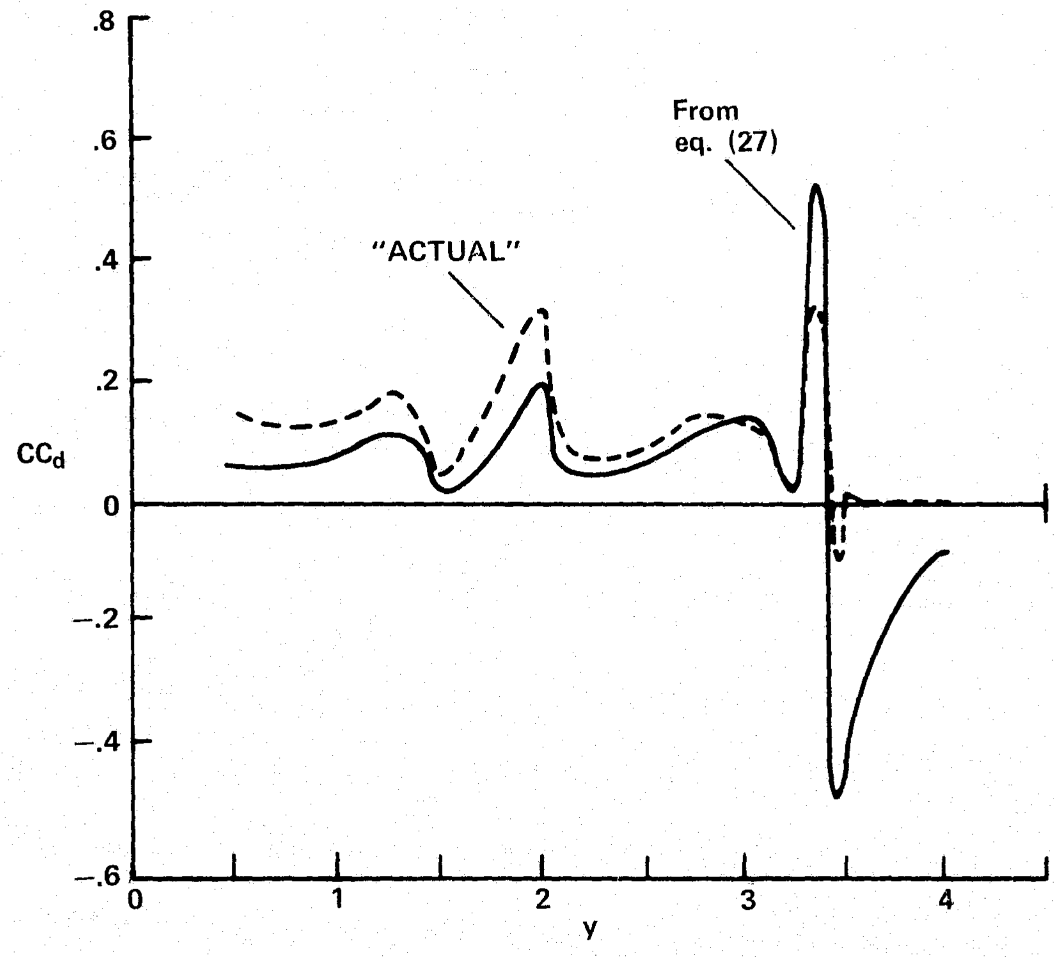

Figure 19.- Comparison of "actual" induced drag, $-u_z(cc_\ell)_{meas}$, and the distribution computed from equation (27). Elliptic loading. $C_L = 1.66$.

APPENDIX A

ANALYSIS OF THE SHEAR STRESS TERMS IN THE INTEGRAL MOMENTUM EQUATION

To determine the relative importance of the shear forces on the control surface (figs. 1 and 2) compared with the other terms in equation (3), we assume that it is valid to conduct a two-dimensional analysis. The orders of magnitude and the trends should be similar in three dimensions.

Momentum Equation in Two Dimensions

In the two-dimensional approximation of the flow, equation (3) simplifies to

$$-\int_{L_1} \rho \vec{u} u_x \, dz + \int_{L_2} \rho \vec{u} u_z \, dx + \int_{L_3} \rho \vec{u} u_x \, dz - \int_{L_4} \rho \vec{u} u_z \, dx$$

$$= \int_{L_1} p\hat{x} \, dz - \int_{L_2} p\hat{z} \, dx - \int_{L_3} p\hat{x} \, dz + \int_{L_4} p\hat{z} \, dx - D_p\hat{x} - L\hat{z} - D_{sf}\hat{x}$$

$$+ \int_{L_1 \text{ thru } L_4} (\hat{n} \cdot \overleftrightarrow{\tau}) d\ell \qquad \text{(A1)}$$

Separating into components,

$$\left.\begin{aligned}
L &= \int_{L_1} \rho u_x u_z \, dz - \int_{L_2} (\rho u_z^2 + p) dx - \int_{L_3} \rho u_x u_z \, dz + \int_{L_4} (\rho u_z^2 + p) dx \\
&\quad + \int_{L_1 \text{ thru } L_4} (\hat{n} \cdot \overleftrightarrow{\tau})_z \, d\ell \\
D &= D_p + D_{sf} = \int_{L_1} (\rho u_x^2 + p) dz - \int_{L_2} \rho u_x u_z \, dx - \int_{L_3} (\rho u_x^2 + p) dz \\
&\quad + \int_{L_4} \rho u_x u_z \, dx + \int_{L_1 \text{ thru } L_4} (\hat{n} \cdot \overleftrightarrow{\tau})_x \, d\ell
\end{aligned}\right\} \qquad \text{(A2)}$$

Eliminating the static pressures with $p = p_T - (\rho/2)(u_x^2 + u_z^2)$ and nondimensionalizing,

$$\left.\begin{aligned}
c_\ell &= 2\int_{L_1} u_x u_z \, dz - \int_{L_2} (u_z{}^2 - u_x{}^2)dx - 2\int_{L_3} u_x u_z \, dz + \int_{L_4} (u_z{}^2 - u_x{}^2)dx \\
&\quad + \frac{1}{q_\infty c} \int_{L_1 \text{ thru } L_4} (\hat{n} \cdot \overleftrightarrow{\tau})_z \, d\ell \\
c_d &= \int_{L_1} (u_x{}^2 - u_z{}^2)dz - 2\int_{L_2} u_x u_z \, dx - \int_{L_3} (u_x{}^2 - u_z{}^2)dz + 2\int_{L_4} u_x u_z \, dx \\
&\quad + \int_{L_3} \left(\frac{p_0 - p_T}{q_\infty}\right)dz + \frac{1}{q_\infty c} \int_{L_1 \text{ thru } L_4} (\hat{n} \cdot \overleftrightarrow{\tau})_x \, d\ell
\end{aligned}\right\} \quad \text{(A3)}$$

Modeling of the Shear Stress Tensor

The shear stress tensor is written in general form as

$$\overleftrightarrow{\tau} = \mu \begin{pmatrix} 2\dfrac{\partial u_x}{\partial x} & \dfrac{\partial u_x}{\partial z} + \dfrac{\partial u_z}{\partial x} \\ \dfrac{\partial u_x}{\partial z} + \dfrac{\partial u_z}{\partial x} & 2\dfrac{\partial u_z}{\partial z} \end{pmatrix}$$

If the flow is represented (fig. A-1) by a superposition of the free-stream flow, a bound vortex, and a viscous wake,

$$\vec{u} = \left(V_\infty + u_x{}^w + \frac{\Gamma}{2\pi}\frac{z}{r^2}\right)\hat{x} + \left(u_y{}^w - \frac{\Gamma}{2\pi}\frac{x}{r^2}\right)\hat{z}$$

where Γ is the strength of the bound vortex and the superscript w denotes a perturbation term due to the viscous wake. These wake terms vanish everywhere except in the wake region. The stress tensor now becomes,

$$\overleftrightarrow{\tau} = \mu \begin{pmatrix} 2\dfrac{\partial u_x{}^w}{\partial x} - \dfrac{2\Gamma}{\pi}\dfrac{xz}{r^4} & \dfrac{\partial u_x{}^w}{\partial z} + \dfrac{\partial u_z{}^w}{\partial x} + \dfrac{\Gamma}{\pi}\dfrac{x^2 - z^2}{r^4} \\ \dfrac{\partial u_x{}^w}{\partial z} + \dfrac{\partial u_z{}^w}{\partial x} + \dfrac{\Gamma}{\pi}\dfrac{x^2 - z^2}{r^4} & 2\dfrac{\partial u_z{}^w}{\partial z} + \dfrac{2\Gamma}{\pi}\dfrac{xz}{r^4} \end{pmatrix} \quad \text{(A4)}$$

Since the trace of the matrix remains invariant and vanishes for an incompressible flow,

$$\frac{\partial u_x^w}{\partial x} + \frac{\partial u_z^w}{\partial z} = 0 \tag{A5}$$

as expected.

Evaluation of the Shear Forces

To carry out the integration indicated by the last term in equations (A3), we need to compute $(\hat{x} \cdot \overleftrightarrow{\tau})$ and $(\hat{z} \cdot \overleftrightarrow{\tau})$. Using (A5),

$$\left.\begin{aligned}
(\hat{x} \cdot \overleftrightarrow{\tau}) &= (1 \quad 0)(\overleftrightarrow{\tau}) = \mu \begin{bmatrix} 2\dfrac{\partial u_x^w}{\partial x} - \dfrac{2\Gamma}{\pi}\dfrac{xz}{r^4} \\ \dfrac{\partial u_x^w}{\partial z} + \dfrac{\partial u_z^w}{\partial x} + \dfrac{\Gamma}{\pi}\left(\dfrac{x^2 - z^2}{r^4}\right) \end{bmatrix} \\
(\hat{z} \cdot \overleftrightarrow{\tau}) &= (0 \quad 1)(\overleftrightarrow{\tau}) = \mu \begin{bmatrix} \dfrac{\partial u_x^w}{\partial z} + \dfrac{\partial u_z^w}{\partial x} + \dfrac{\Gamma}{\pi}\left(\dfrac{x^2 - z^2}{r^4}\right) \\ -2\dfrac{\partial u_x^w}{\partial x} + \dfrac{2\Gamma}{\pi}\dfrac{xz}{r^4} \end{bmatrix}
\end{aligned}\right\} \tag{A6}$$

Equation (A6) is valid everywhere. If, however, it is assumed that the shearing due to the viscous wake is only significant over a localized region along L_3, then we have elsewhere,

$$(\hat{x} \cdot \overleftrightarrow{\tau}) = \frac{\mu\Gamma}{\pi}\begin{pmatrix} -2\dfrac{xz}{r^4} \\ \dfrac{x^2 - z^2}{r^4} \end{pmatrix} \quad \text{and} \quad (\hat{z} \cdot \overleftrightarrow{\tau}) = \frac{\mu\Gamma}{\pi}\begin{pmatrix} \dfrac{x^2 - z^2}{r^4} \\ 2\dfrac{xz}{r^4} \end{pmatrix} \tag{A7}$$

The shear terms in equations (A3) may now be written as

$$\int_{L_1 \text{ thru } L_4} (\hat{n} \cdot \overleftrightarrow{\tau})_z \, d\ell = -\int_{L_1} (\hat{x} \cdot \overleftrightarrow{\tau})_z \, dz + \int_{L_2} (\hat{z} \cdot \overleftrightarrow{\tau})_z \, dx + \int_{L_3} (\hat{x} \cdot \overleftrightarrow{\tau})_z \, dz$$
$$- \int_{L_4} (\hat{z} \cdot \overleftrightarrow{\tau})_z \, dx \tag{A8}$$

$$\int_{L_1 \text{ thru } L_4} (\hat{n} \cdot \overleftrightarrow{\tau})_x \, d\ell = -\int_{L_1} (\hat{x} \cdot \overleftrightarrow{\tau})_x \, dz + \int_{L_2} (\hat{z} \cdot \overleftrightarrow{\tau})_x \, dx + \int_{L_3} (\hat{x} \cdot \overleftrightarrow{\tau})_x \, dz$$
$$- \int_{L_4} (\hat{z} \cdot \overleftrightarrow{\tau})_x \, dx \tag{A9}$$

The integrations are greatly simplified and no generality is lost if we choose the symmetric controur in figure A-2.

Using equations (A6) and (A7) in (A8),

$$\int_{L_1 \text{ thru } L_4} (\hat{n} \cdot \overleftrightarrow{\tau})_z \, d\ell = \frac{\mu\Gamma}{\pi}\left[-\int_{-\kappa}^{\kappa} \frac{x^2 - z^2}{r^4}\, dz\right]_{x=-\varepsilon} + \frac{\mu\Gamma}{\pi}\left[\int_{-\varepsilon}^{\varepsilon} \frac{2xz}{r^4}\, dx\right]_{z=\kappa}$$

$$+ \frac{\mu\Gamma}{\pi}\left[\int_{-\kappa}^{\kappa} \frac{x^2 - z^2}{r^4}\, dz\right]_{x=\varepsilon} + \mu\left[\int_{-\kappa}^{\kappa}\left(\frac{\partial u_x^{\,w}}{\partial z} + \frac{\partial u_z^{\,w}}{\partial x}\right)dz\right]_{x=\varepsilon}$$

$$+ \frac{\mu\Gamma}{\pi}\left[-\int_{-\varepsilon}^{\varepsilon} \frac{2xz}{r^4}\, dx\right]_{z=-\kappa}$$

Since the integrands of the first and third terms are even in x and z, these terms cancel. Also, since the integrands of the second and last terms are odd in x and z, these terms cancel. Equation (A9) is analyzed similarly and the result is

$$\left.\begin{aligned} \int_{L_1 \text{ thru } L_4} (\hat{n} \cdot \overleftrightarrow{\tau})_z \, d\ell &= \mu\int_{L_3}\left(\frac{\partial u_x^{\,w}}{\partial z} + \frac{\partial u_z^{\,w}}{\partial x}\right)dz \\ \int_{L_1 \text{ thru } L_4} (\hat{n} \cdot \overleftrightarrow{\tau})_x \, d\ell &= 2\mu\int_{L_3}\frac{\partial u_x^{\,w}}{\partial x}\, dz \end{aligned}\right\} \quad \text{(A10)}$$

The last terms in (A3) may, therefore, be written nondimensionally as

$$\left.\begin{aligned} \frac{1}{q_\infty c}\int_{L_1 \text{ thru } L_4} (\hat{n} \cdot \overleftrightarrow{\tau})_z \, d\ell &= \frac{2}{Re_c}\int_{L_3}\left(\frac{\partial u_x^{\,w}}{\partial z} + \frac{\partial u_z^{\,w}}{\partial x}\right)dz \\ \frac{1}{q_\infty c}\int_{L_1 \text{ thru } L_4} (\hat{n} \cdot \overleftrightarrow{\tau})_x \, d\ell &= \frac{4}{Re_c}\int_{L_3}\frac{\partial u_x^{\,w}}{\partial x}\, dz \end{aligned}\right\} \quad \text{(A11)}$$

where $Re_c = \rho c V_\infty/\mu$ is the flow Reynolds number based on wing chord. Clearly, when the velocity gradients in the wake are of order unity, then these terms are negligible for $Re_c >> 1$. This is certainly the case for most wind-tunnel flows.

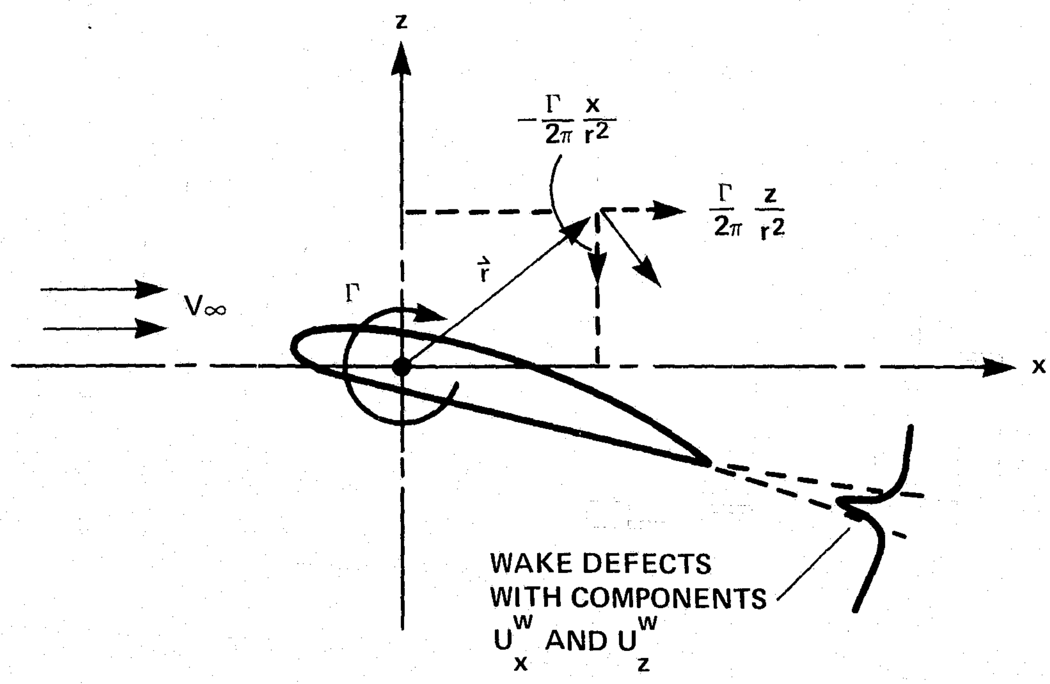

Figure A-1.- Flow modeled by superposition of free stream, bound vortex, and viscous wake.

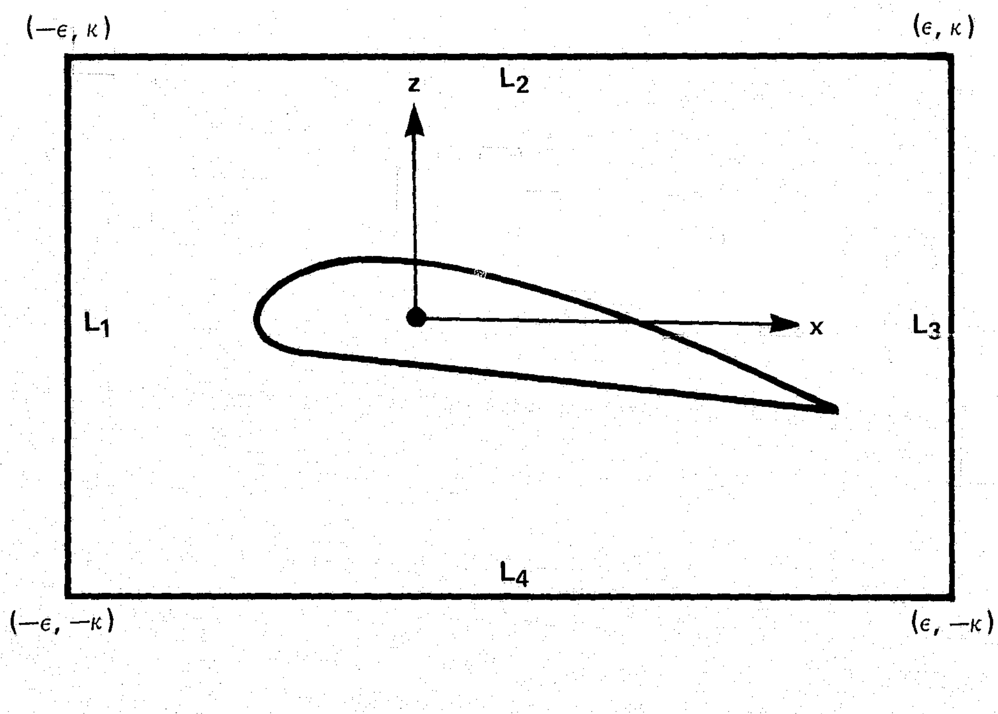

Figure A-2.- Symmetrical integration contour.

APPENDIX B

EXPANSION OF THE SURFACE INTEGRALS IN EQUATIONS (9)

The terms that are to be expanded are

$$-2\int_S \frac{\partial}{\partial y}(u_y u_z)dx\,dz$$
$$-2\int_S \frac{\partial}{\partial y}(u_x u_y)dx\,dz \tag{B1}$$

Using the chain rule and then using the principle of continuity, (B1) becomes

$$2\iint_S u_z \frac{\partial u_x}{\partial x}dx\,dz + 2\iint_S u_z \frac{\partial u_z}{\partial z}dx\,dz - 2\iint_S u_y \frac{\partial u_z}{\partial y}dx\,dz \tag{B2}$$

$$2\iint_S u_x \frac{\partial u_x}{\partial x}dx\,dz + 2\iint_S u_x \frac{\partial u_z}{\partial z}dx\,dz - 2\iint_S u_y \frac{\partial u_x}{\partial y}dx\,dz \tag{B3}$$

where the surface integrations are now shown explicitly by the double integral.

Evaluation of (B2)

First term: integrate by parts to get

$$2\iint_S u_z \frac{\partial u_x}{\partial x}dx\,dz = 2\int\left\{u_x u_z\Big|_{x\text{ on }L_1}^{x\text{ on }L_3} - \int u_x \frac{\partial u_z}{\partial x}dx\right\}dz$$

$$= 2\int_{L_3} u_x u_z\,dz - 2\int_{L_1} u_x u_z\,dz - 2\iint_S u_x \frac{\partial u_z}{\partial x}dx\,dz$$

Second term:

$$2\iint_S u_z \frac{\partial u_z}{\partial z}dx\,dz = \int\left(\int \frac{\partial u_z^{\,2}}{\partial z}dz\right)dx = \int u_z^{\,2}\Big|_{z\text{ on }L_4}^{z\text{ on }L_2}dx$$

$$= \int_{L_2} u_z^{\,2}\,dx - \int_{L_4} u_z^{\,2}\,dx$$

Third term:

$$-2\iint_S u_y \frac{\partial u_z}{\partial y}\,dx\,dz = -2\iint_S u_y\left(\frac{\partial u_z}{\partial y} - \frac{\partial u_y}{\partial z}\right)dx\,dz - 2\iint_S u_y \frac{\partial u_y}{\partial z}\,dx\,dz$$

$$= -2\iint_S u_y\left(\frac{\partial u_z}{\partial y} - \frac{\partial u_y}{\partial z}\right)dx\,dz - \int_{L_2} u_y^{\,2}\,dx + \int_{L_4} u_y^{\,2}\,dx$$

(B2) is now written as

$$-2\int_{L_1} u_x u_z\,dz + \int_{L_2}(u_z^{\,2} - u_y^{\,2})dx + 2\int_{L_3} u_x u_z\,dz - \int_{L_4}(u_z^{\,2} - u_y^{\,2})dx$$

$$- 2\iint_S u_y\left(\frac{\partial u_z}{\partial y} - \frac{\partial u_y}{\partial z}\right)dx\,dz - 2\iint_S u_x \frac{\partial u_z}{\partial x}\,dx\,dz$$

Noting that $2\iint_S u_x \frac{\partial u_x}{\partial z}\,dx\,dz = \int_{L_2} u_x^{\,2}\,dx - \int_{L_4} u_x^{\,2}\,dx$, we now have

$$-2\iint_S \frac{\partial}{\partial y}(u_y u_z)dx\,dz = -2\int_{L_1} u_x u_z\,dz + \int_{L_2}(u_z^{\,2} - u_x^{\,2} - u_y^{\,2})dx + 2\int_{L_3} u_x u_z\,dz$$

$$- \int_{L_4}(u_z^{\,2} - u_x^{\,2} - u_y^{\,2})dx + 2\iint_S u_x\left(\frac{\partial u_x}{\partial z} - \frac{\partial u_z}{\partial x}\right)dx\,dz$$

$$- 2\iint_S u_y\left(\frac{\partial u_z}{\partial y} - \frac{\partial u_y}{\partial z}\right)dx\,dz \qquad \text{(B4)}$$

Evaluation of (B3)

First term:

$$2\iint_S u_x \frac{\partial u_x}{\partial x}\,dx\,dz = \int_{L_3} u_x^{\,2}\,dz - \int_{L_1} u_x^{\,2}\,dz$$

Second term: integrate by parts to get

$$2\iint_S u_x \frac{\partial u_z}{\partial z}\,dx\,dz = 2\int\left(u_x u_z\Big|_{z \text{ on } L_4}^{z \text{ on } L_2} - \int u_z \frac{\partial u_x}{\partial z}\,dz\right)dx$$

$$= 2\int_{L_2} u_x u_z\,dx - 2\int_{L_4} u_x u_z\,dx - 2\iint_S u_z \frac{\partial u_x}{\partial z}\,dx\,dz$$

Third term:

$$-2\iint_S u_y \frac{\partial u_x}{\partial y}\, dx\, dz = -2\iint_S u_y \left(\frac{\partial u_x}{\partial y} - \frac{\partial u_y}{\partial x}\right) dx\, dz - 2\iint_S u_y \frac{\partial u_y}{\partial x}\, dx\, dz$$

$$= -2\iint_S u_y \left(\frac{\partial u_x}{\partial y} - \frac{\partial u_y}{\partial x}\right) dx\, dz - \int_{L_3} u_y^2\, dz + \int_{L_1} u_y^2\, dz$$

(B3) now is written as

$$-\int_{L_1} (u_x^2 - u_y^2) dz + 2\int_{L_2} u_x u_z\, dx + \int_{L_3} (u_x^2 - u_y^2) dz - 2\int_{L_4} u_x u_z\, dx$$

$$- 2\iint_S u_y \left(\frac{\partial u_x}{\partial y} - \frac{\partial u_y}{\partial x}\right) dx\, dz - 2\iint_S u_z \frac{\partial u_x}{\partial z}\, dx\, dz$$

Noting that $2\iint_S u_z \frac{\partial u_z}{\partial x}\, dx\, dz = \int_{L_3} u_z^2\, dz - \int_{L_1} u_z^2\, dz$, we obtain,

$$-2\iint_S \frac{\partial}{\partial y} (u_x u_y) dx\, dz = -\int_{L_1} (u_x^2 - u_y^2 - u_z^2) dz + 2\int_{L_2} u_x u_z\, dx$$

$$+ \int_{L_3} (u_x^2 - u_y^2 - u_z^2) dz - 2\int_{L_4} u_x u_z\, dx$$

$$+ 2\iint_S u_y \left(\frac{\partial u_y}{\partial x} - \frac{\partial u_x}{\partial y}\right) dx\, dz - 2\iint_S u_z \left(\frac{\partial u_x}{\partial z} - \frac{\partial u_z}{\partial x}\right) dx\, dz \qquad \text{(B5)}$$

APPENDIX C

THE INDUCED VELOCITY AT A POINT (x, y, z) DUE TO A HORSESHOE VORTEX

To calculate the induced velocity at a point P, we use the Biot-Savart Induction Law

$$d\vec{u} = \frac{\Gamma}{4\pi} \frac{d\vec{s} \times \vec{r}}{r^3} \tag{C1}$$

where the vector quantities are defined by figure C-1. The vector $\vec{r}$ from the source element of vorticity of length $d\vec{s}$ to point P is either $\vec{r}_B$, $\vec{r}_+$, or $\vec{r}_-$, depending on the section of the horseshoe being considered. It can be shown that the induced velocity at P due to the bound vortex is given by

$$\vec{u}_B = \frac{\Gamma}{4\pi} \left[\frac{y_0 + y}{\sqrt{x^2 + (y_0 + y)^2 + z^2}} + \frac{y_0 - y}{\sqrt{x^2 + (y_0 - y)^2 + z^2}} \right] \left(x^2 + z^2\right)^{-1} (z\hat{x} - x\hat{z}) \tag{C2}$$

The induced velocity at P due to the trailing portion of the horseshoe on the positive y-side of the origin is given by

$$\vec{u}_+ = -\frac{\Gamma}{4\pi} \left[\frac{x}{\sqrt{x^2 + (y_0 - y)^2 + z^2}} + 1 \right] \left[(y_0 - y)^2 + z^2 \right]^{-1} \left[z\hat{y} + (y_0 - y)\hat{z} \right] \tag{C3}$$

and the induced velocity at P due to the trailing portion on the negative y-side of the origin is given by

$$\vec{u}_- = \frac{\Gamma}{4\pi} \left[\frac{x}{\sqrt{x^2 + (y_0 + y)^2 + z^2}} + 1 \right] \left[(y_0 + y)^2 + z^2 \right]^{-1} \left[z\hat{y} - (y_0 + y)\hat{z} \right] \tag{C4}$$

Combining (C2), (C3), and (C4) and separating components,

$$\begin{aligned} u_x &= V_\infty + \frac{\Gamma}{4\pi} Az \\ u_y &= -\frac{\Gamma}{4\pi} (B - C) z \\ u_z &= -\frac{\Gamma}{4\pi} \left[Ax + (y_0 - y)B + (y_0 + y)C \right] \end{aligned} \tag{C5}$$

where

$$A = \left[\frac{y_0 + y}{\sqrt{x^2 + (y_0 + y)^2 + z^2}} + \frac{y_0 - y}{\sqrt{x^2 + (y_0 - y)^2 + z^2}} \right] [x^2 + z^2]^{-1}$$

$$B = \left[\frac{x}{\sqrt{x^2 + (y_0 - y)^2 + z^2}} + 1 \right] [(y_0 - y)^2 + z^2]^{-1}$$

$$C = \left[\frac{x}{\sqrt{x^2 + (y_0 + y)^2 + z^2}} + 1 \right] [(y_0 + y)^2 + z^2]^{-1}$$

Nondimensionalizing u by V_∞, and x, y, z by $\bar{c}$,

$$u_x = 1 + \gamma A z$$

$$u_y = \gamma (C - B) z \tag{C6}$$

$$u_z = -\gamma [Ax + B(y_0 - y) + C(y_0 + y)]$$

with A, B, and C unchanged but all terms now nondimensional, and $\gamma = cc_\ell/8\pi$ is the nondimensional vortex strength.

To protect against singularities in the wake, a finite core diameter r_c is specified for the trailing portions of the horseshoe. This is accomplished by replacing

$$B = \frac{1}{r_c^{\,2}} \left[\frac{x}{\sqrt{x^2 + (y_0 - y)^2 + z^2}} + 1 \right] \quad \text{if} \quad (y_0 - y)^2 + z^2 \leqslant r_c^{\,2}$$

$$C = \frac{1}{r_c^{\,2}} \left[\frac{x}{\sqrt{x^2 + (y_0 + y)^2 + z^2}} + 1 \right] \quad \text{if} \quad (y_0 + y)^2 + z^2 \leqslant r_c^{\,2}$$

To allow for downward deflection of the wake, we assume that in a superposition of N horseshoes, each vortex trails downward at angle $\varepsilon_i (i = 1, 2 \ldots, N)$ induced by the other vortices (see fig. C-2).

We want to calculate the downwash velocity u_{z_i} induced on the bound vortex at location y_{0_i} where Γ_i is shed. To do this we again use the Biot-Savart Induction Law. Assuming that all other vortices trail straight back, it can be shown that the induced velocity at y_{0_i} due to the other vortices on the (+) y-side of the centerline is given by

$$u_{z_+} = \frac{1}{4\pi} \sum_{\substack{j=1 \\ j \neq i}}^{N} \frac{\Gamma_j}{\left(y_{0_i} - y_{0_j}\right)} \tag{C7}$$

The induced velocity at y_{0_i} due to all vortices on the (-) y-side of the centerline is given by

$$u_{z_-} = -\frac{1}{4\pi} \sum_{j=1}^{N} \frac{\Gamma_j}{\left(y_{0_i} + y_{0_j}\right)} \tag{C8}$$

Combining (C7) and (C8), the total induced downwash is

$$u_{z_i} = \frac{1}{4\pi} \left[\sum_{\substack{j=1 \\ i \neq j}}^{N} \frac{2\Gamma_j y_{0_j}}{y_{0_i}^2 - y_{0_j}^2} - \frac{\Gamma_i}{2y_{0_i}} \right] \tag{C9}$$

If we take the induced angle as $\varepsilon_i = \frac{|u_{z_i}|}{V_\infty}$, then in nondimensional form,

$$\varepsilon_i = -\sum_{\substack{j=1 \\ i \neq j}}^{N} \frac{2\gamma_j y_{0_j}}{y_{0_i}^2 - y_{0_j}^2} - \frac{\gamma_i}{2y_{0_i}} \tag{C10}$$

where

$$\gamma_i = \frac{\Gamma_i}{4\pi V_\infty \bar{c}} = \frac{(cc_\ell)_i}{8\pi}$$

The flow field is now generated in the following manner:

(i) Specify (x, y, z) where the velocity is desired.

(ii) Determine rotated coordinates (x', y', z') for the ith horseshoe by

$$\begin{pmatrix} x' \\ y' \\ z' \end{pmatrix} = \begin{pmatrix} \cos\varepsilon_i & 0 & -\sin\varepsilon_i \\ 0 & 1 & 0 \\ \sin\varepsilon_i & 0 & \cos\varepsilon_i \end{pmatrix} \begin{pmatrix} x \\ y \\ z \end{pmatrix}$$

with ε_i computed by equation (C10).

(iii) Compute velocities in the rotated coordinate system, (u_x', u_y', u_z'), using equation (C6).

(iv) Compute (u_x, u_y, u_z) by rotating back to the x, y, z frame

$$\begin{pmatrix} u_x \\ u_y \\ u_z \end{pmatrix} = \begin{pmatrix} \cos \varepsilon_i & 0 & \sin \varepsilon_i \\ 0 & 1 & 0 \\ -\sin \varepsilon_i & 0 & \cos \varepsilon_i \end{pmatrix} \begin{pmatrix} u_x' \\ u_y' \\ u_z' \end{pmatrix}$$

Steps (i) through (iv) are carried out for each horseshoe and the total induced velocity at P is then obtained by linear superposition.

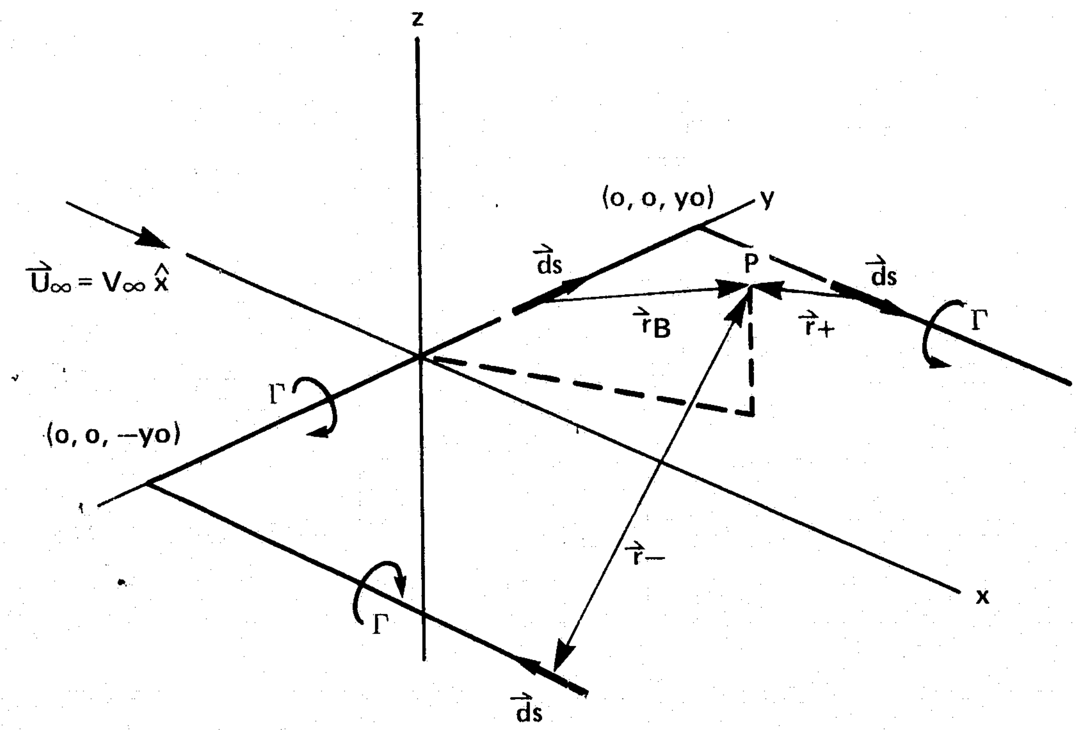

Figure C-1.- Horseshoe vortex and coordinate system.

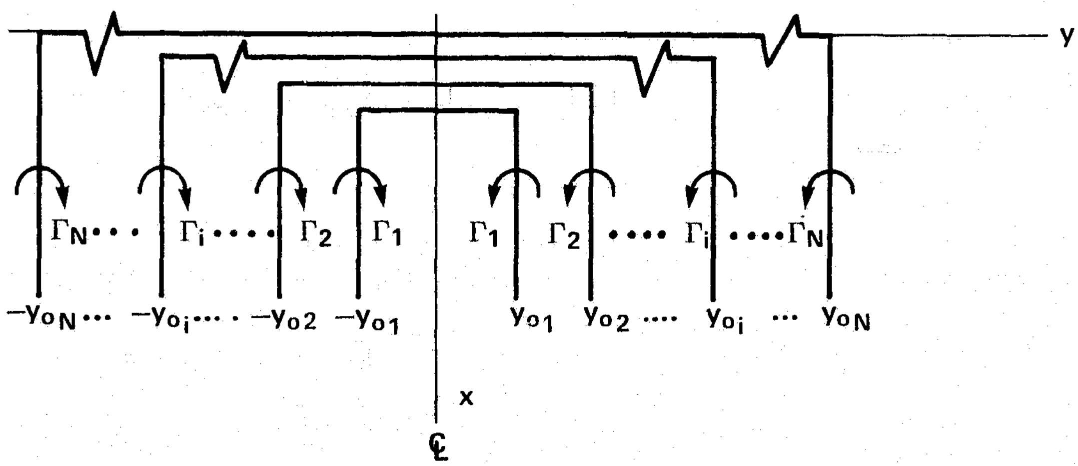

Figure C-2.- Superposition of N horseshoe vortices.

APPENDIX D

DATA SUMMARY

<u>Legend</u>

+ = "Measured" cc_ℓ

o = Corrected cc_ℓ

--- = "Actual" loading

All data are for $x = 0.9$.

ENTEP PUN NUMEEP: 35
TPAVERSE DISTANCE= 0.50 CHOPDS
TOTAL WING LIFT COEFFICIENT= 1.08
LOCATION OF EQUIVALENT VORTEX= 3.05
STRENGTH OF EQUIVALENT VORTEX= 1.28
CORRECTION ACCURACY= 78.1 PERCENT
ACCURACY IN TOTAL CL= 1.0 PERCENT

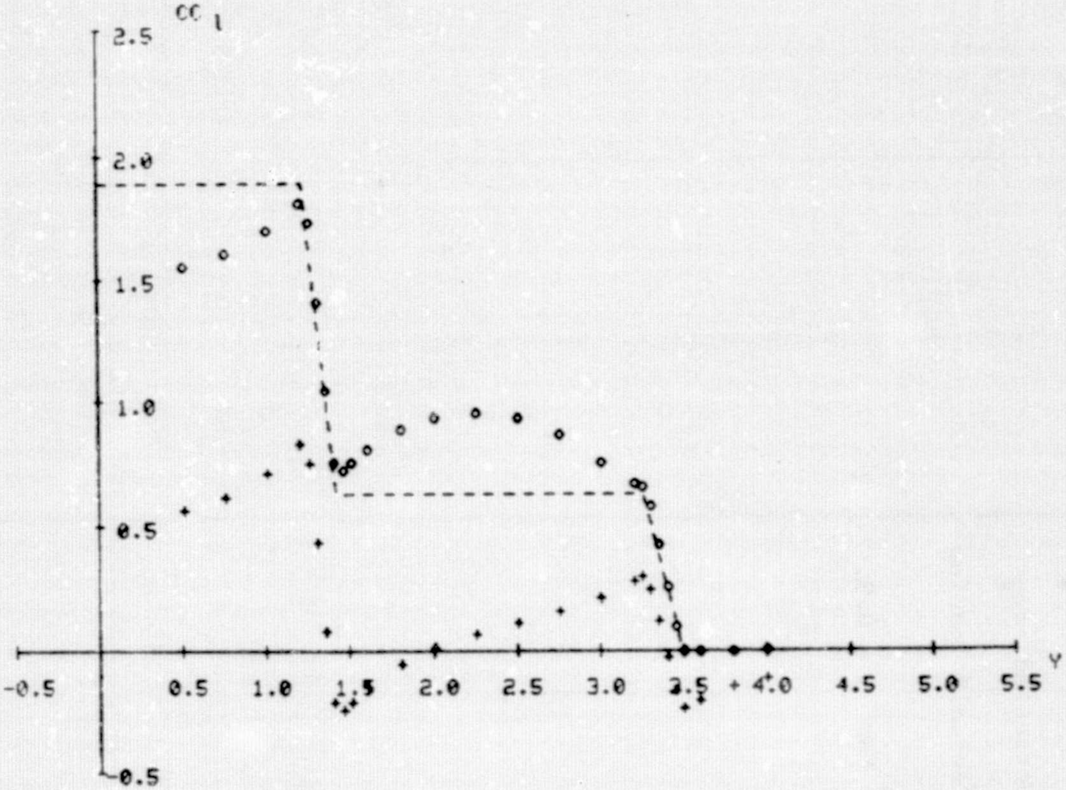

Figure D-1

ENTER RUN NUMBER: 36
TRAVERSE DISTANCE= 0.75 CHORDS

TOTAL WING LIFT COEFFICIENT= 1.03

LOCATION OF EQUIVALENT VORTEX= 2.91

STRENGTH OF EQUIVALENT VORTEX= 1.35

CORRECTION ACCURACY= 85.1 PERCENT

ACCURACY IN TOTAL CL= 1.0 PERCENT

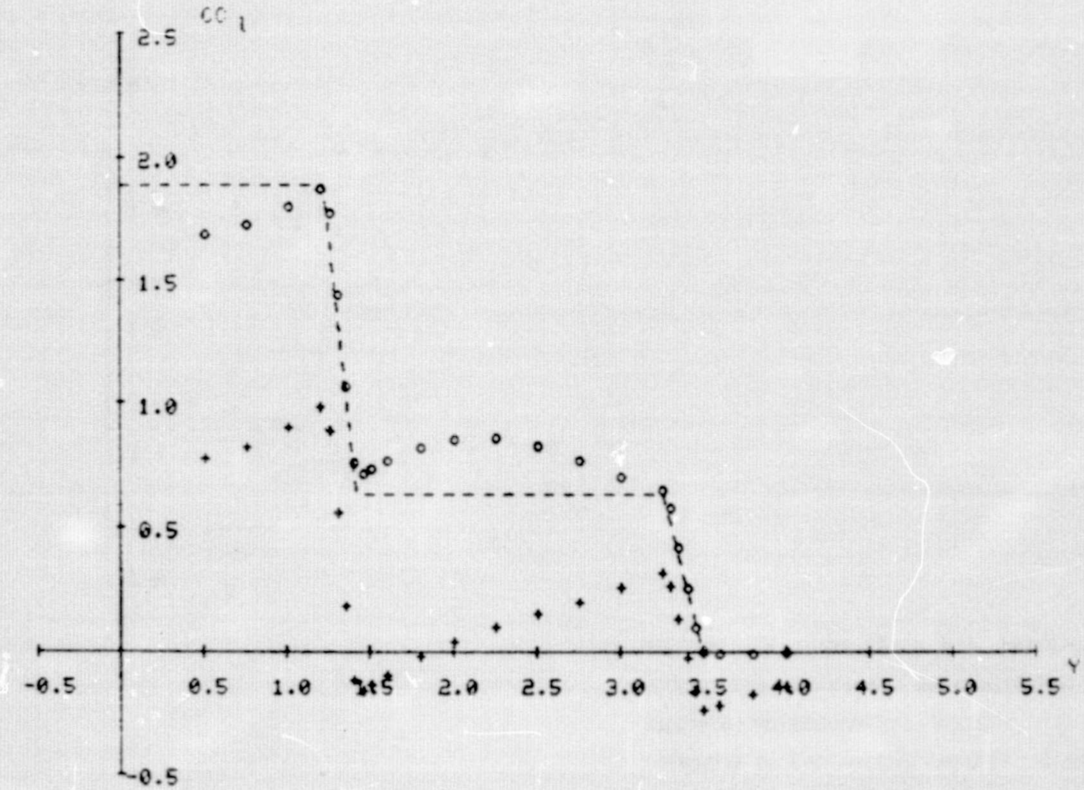

Figure D-2

ENTER RUN NUMBER: 30

TRAVERSE DISTANCE= 1.00 CHORDS

TOTAL WING LIFT COEFFICIENT= 1.08

LOCATION OF EQUIVALENT VORTEX= 2.79

STRENGTH OF EQUIVALENT VORTEX= 1.42

CORRECTION ACCURACY= 89.7 PERCENT

ACCURACY IN TOTAL CL= 1.0 PERCENT

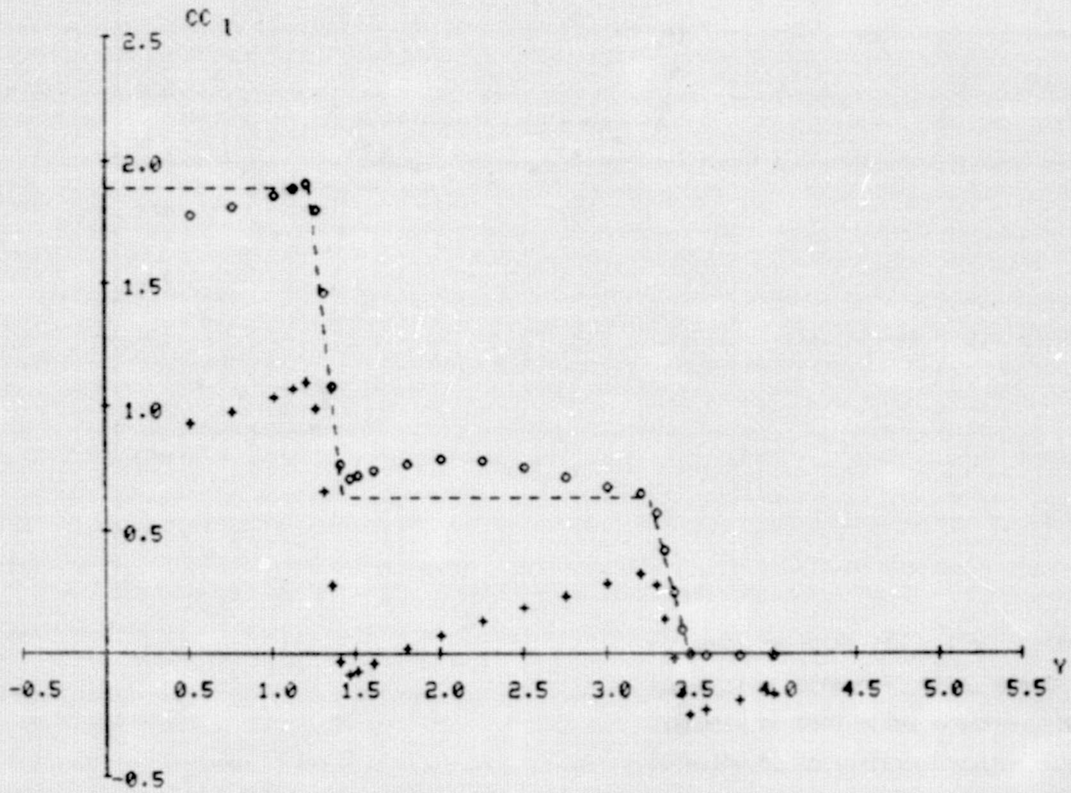

Figure D-3

ENTER RUN NUMBER: 37
TRAVERSE DISTANCE= 1.50 CHORDS
TOTAL WING LIFT COEFFICIENT= 1.08
LOCATION OF EQUIVALENT VORTEX= 2.58
STRENGTH OF EQUIVALENT VORTEX= 1.54
CORRECTION ACCURACY= 94.3 PERCENT
ACCURACY IN TOTAL CL= 1.0 PERCENT

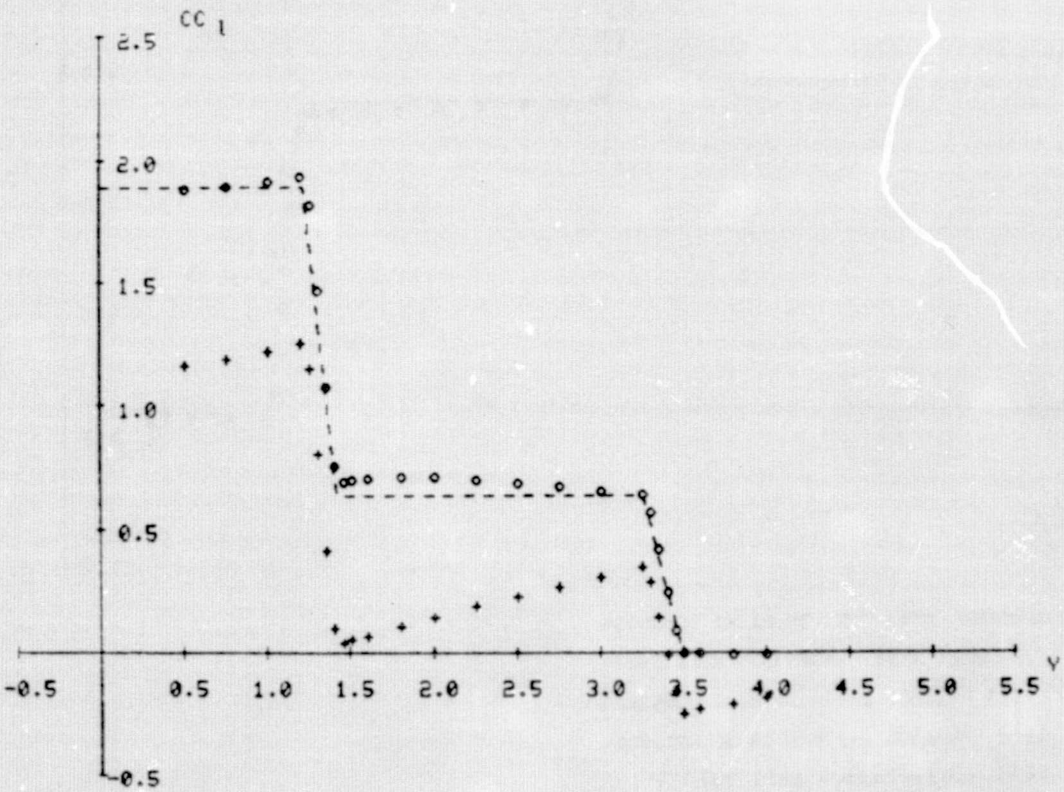

Figure D-4

ENTER RUN NUMBER: 34
TRAVERSE DISTANCE= 2.00 CHORDS

TOTAL WING LIFT COEFFICIENT= 1.08

LOCATION OF EQUIVALENT VORTEX= 2.41

STRENGTH OF EQUIVALENT VORTEX= 1.64

CORRECTION ACCURACY= 96.1 PERCENT

ACCURACY IN TOTAL CL= 1.0 PERCENT

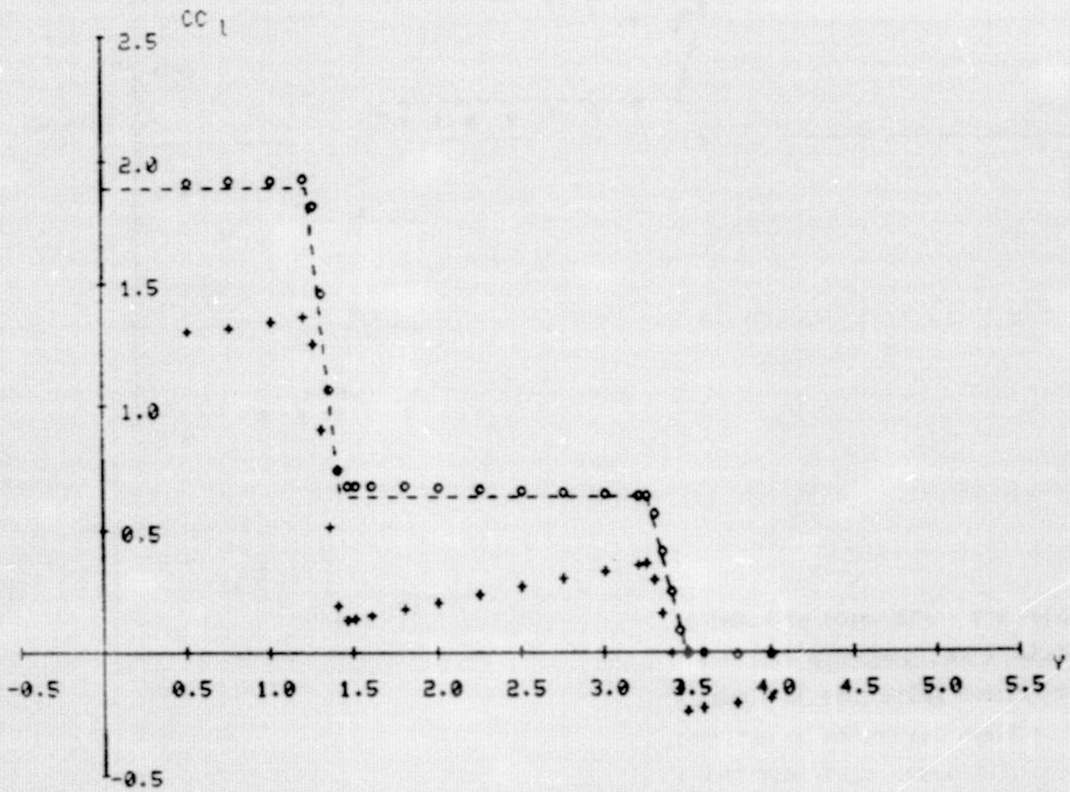

Figure D-5

ENTER RUN NUMBER: 06
TRAVERSE DISTANCE= 0.30 CHORDS

TOTAL WING LIFT COEFFICIENT= 1.12

LOCATION OF EQUIVALENT VORTEX= 3.15

STRENGTH OF EQUIVALENT VORTEX= 1.21

CORRECTION ACCURACY= 70.6 PERCENT

ACCURACY IN TOTAL CL= 4.0 PERCENT

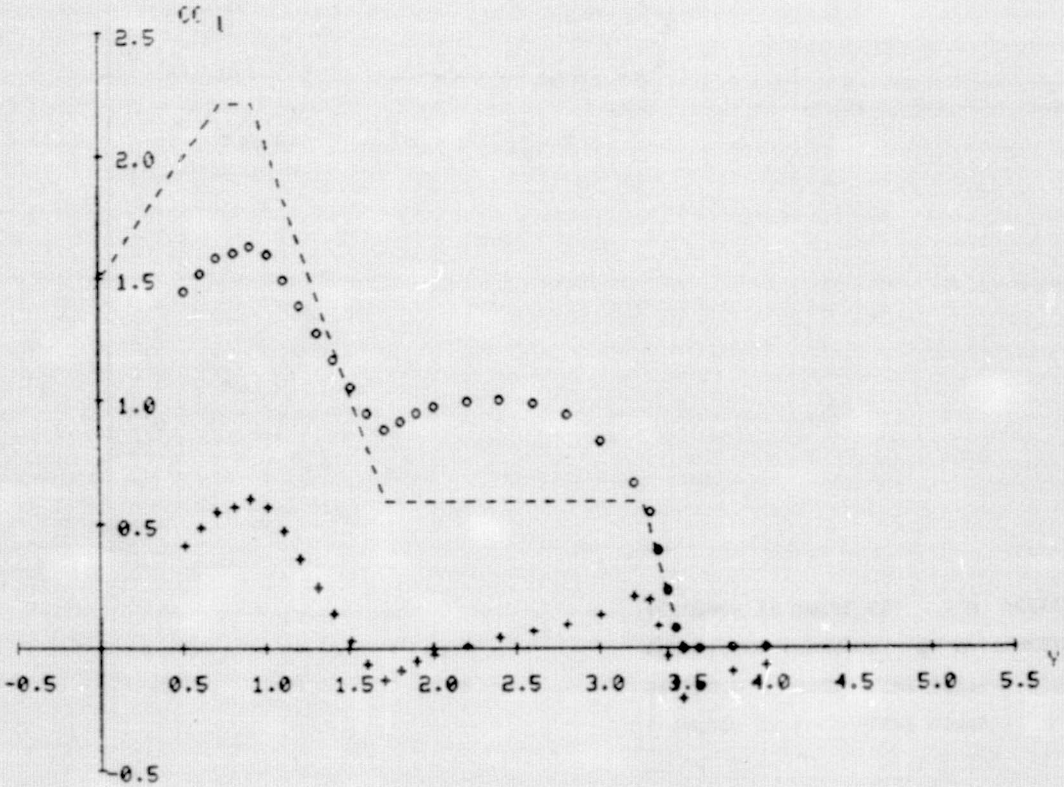

Figure D-6

ENTER RUN NUMBER: 03
TRAVERSE DISTANCE= 0.50 CHORDS

TOTAL WING LIFT COEFFICIENT= 1.12

LOCATION OF EQUIVALENT VORTEX= 3.01

STRENGTH OF EQUIVALENT VORTEX= 1.31

CORRECTION ACCURACY= 80.8 PERCENT

ACCURACY IN TOTAL CL= 1.0 PERCENT

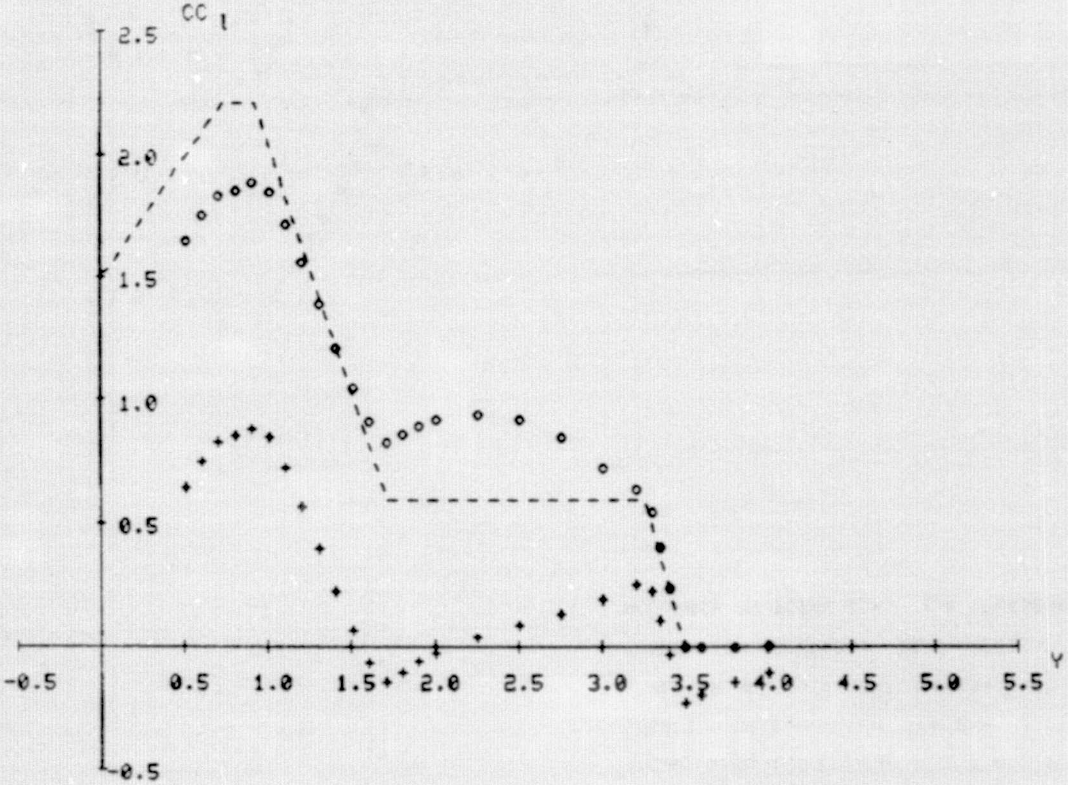

Figure D-7

ENTER RUN NUMBER: 05
TRAVERSE DISTANCE= 0.75 CHORDS

TOTAL WING LIFT COEFFICIENT= 1.12

LOCATION OF EQUIVALENT VORTEX= 2.88

STRENGTH OF EQUIVALENT VORTEX= 1.37

CORRECTION ACCURACY= 8[illegible].8 PERCENT

ACCURACY IN TOTAL CL= 1.0 PERCENT

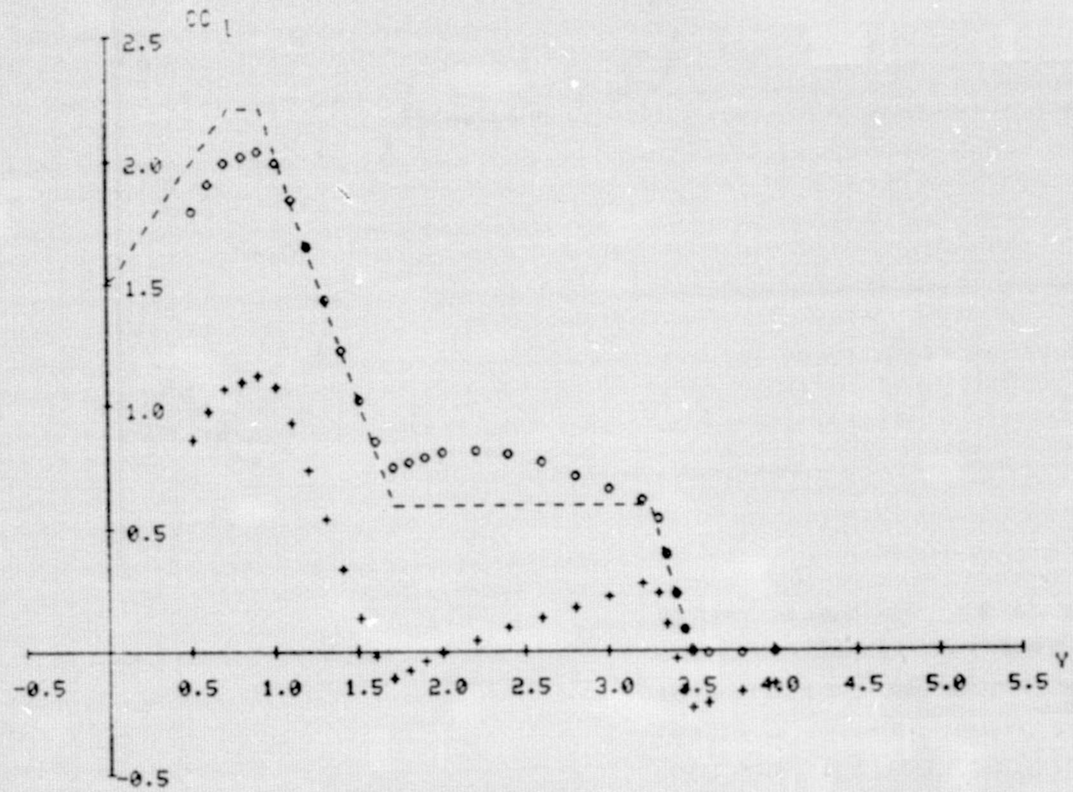

Figure D-8

59

ENTER RUN NUMBER: 01
TRAVERSE DISTANCE= 1.00 CHORDS
TOTAL WING LIFT COEFFICIENT= 1.12
LOCATION OF EQUIVALENT VORTEX= 2.76
STRENGTH OF EQUIVALENT VORTEX= 1.43
CORRECTION ACCURACY= 93.2 PERCENT
ACCURACY IN TOTAL CL= 1.0 PERCENT

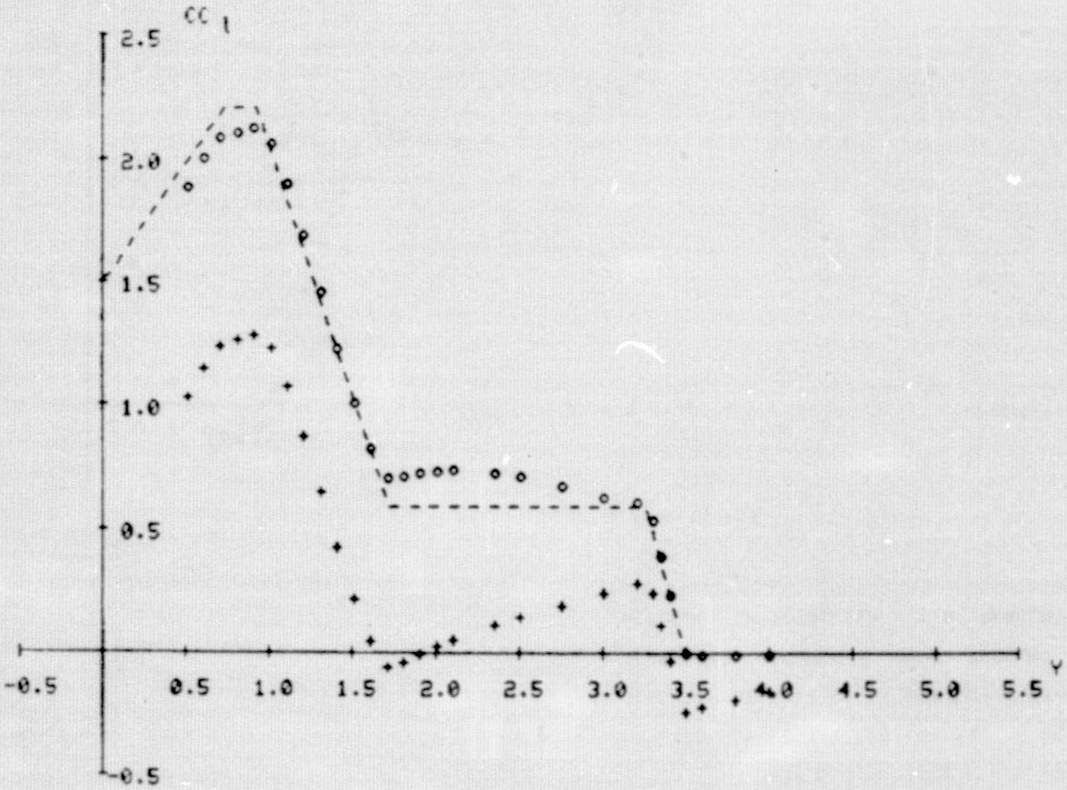

Figure D-9

ENTER RUN NUMBER: 02
TRAVERSE DISTANCE= 1.50 CHORDS

TOTAL WING LIFT COEFFICIENT= 1.12

LOCATION OF EQUIVALENT VORTEX= 2.58

STRENGTH OF EQUIVALENT VORTEX= 1.53

CORRECTION ACCURACY= 97.1 PERCENT

ACCURACY IN TOTAL CL= 1.0 PERCENT

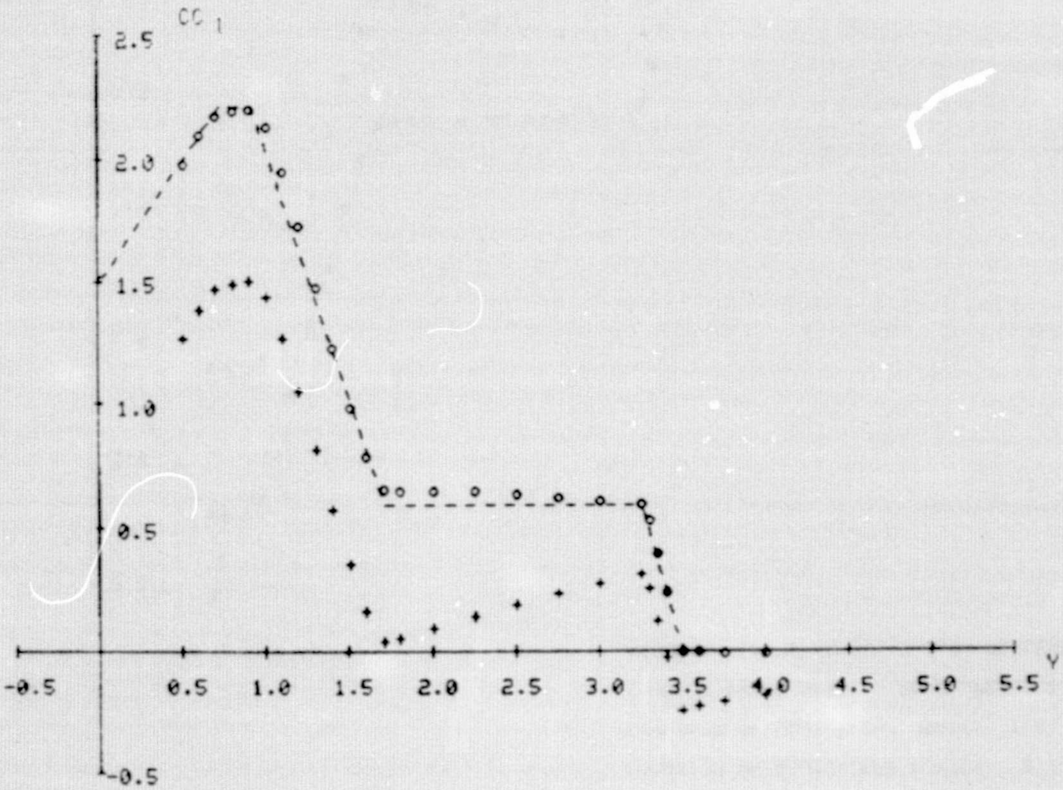

Figure D-10

ENTER RUN NUMBER: 04
TRAVERSE DISTANCE= 2.00 CHORDS
TOTAL WING LIFT COEFFICIENT= 1.12
LOCATION OF EQUIVALENT VORTEX= 2.46
STRENGTH OF EQUIVALENT VORTEX= 1.61
CORRECTION ACCURACY= 96.9 PERCENT
ACCURACY IN TOTAL CL= 1.0 PERCENT

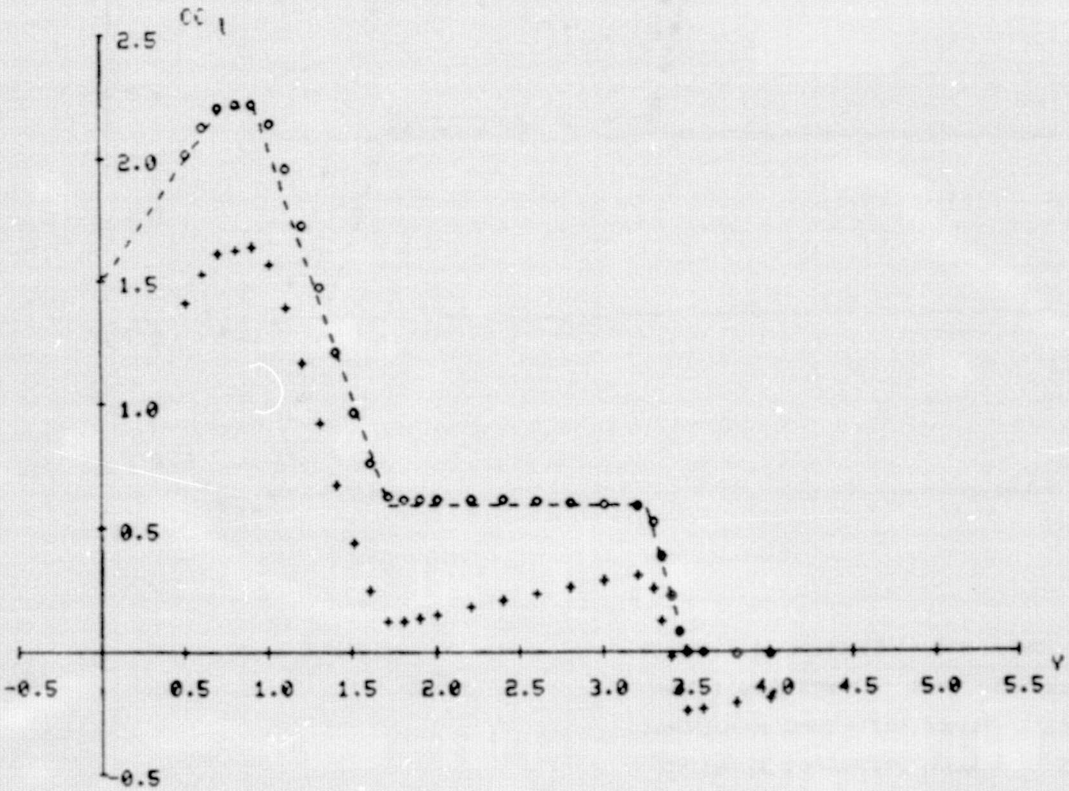

Figure D-11

ENTER RUN NUMBER: 22
TRAVERSE DISTANCE= 0.25 CHORDS

TOTAL WING LIFT COEFFICIENT= 1.19

LOCATION OF EQUIVALENT VORTEX= 3.05

STRENGTH OF EQUIVALENT VORTEX= 1.31

CORRECTION ACCURACY= 83.6 PERCENT

ACCURACY IN TOTAL CL= 4.0 PERCENT

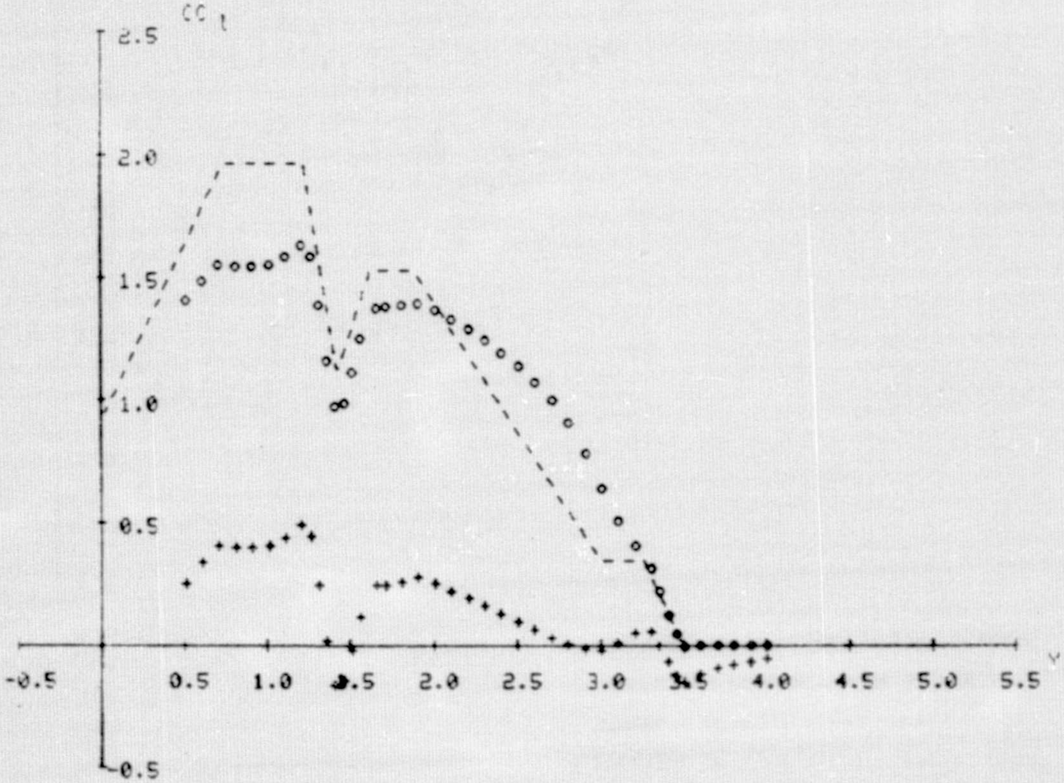

Figure D-12

ENTER RUN NUMBER: 21
TRAVERSE DISTANCE= 0.50 CHORDS
TOTAL WING LIFT COEFFICIENT= 1.19
LOCATION OF EQUIVALENT VORTEX= 2.92
STRENGTH OF EQUIVALENT VORTEX= 1.39
CORRECTION ACCURACY= 90.3 PERCENT
ACCURACY IN TOTAL CL= 1.0 PERCENT

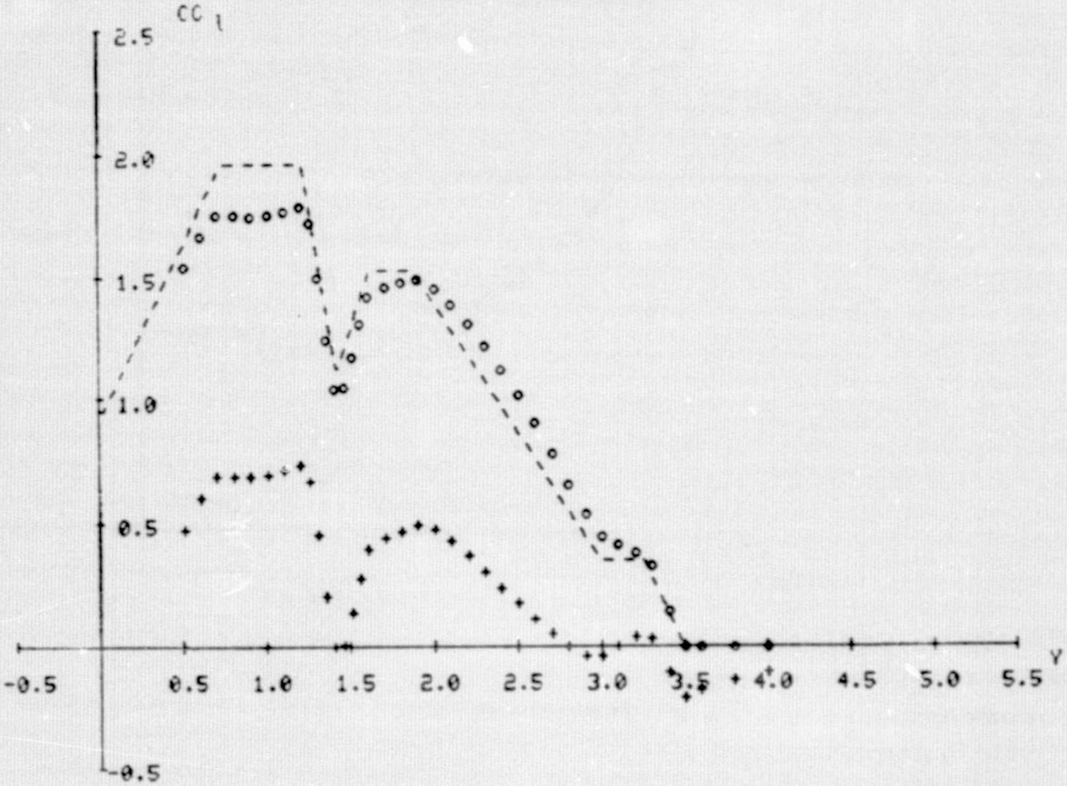

Figure D-13

ENTER RUN NUMBER: 20
TRAVERSE DISTANCE= 1.00 CHORDS
TOTAL WING LIFT COEFFICIENT= 1.19
LOCATION OF EQUIVALENT VORTEX= 2.84
STRENGTH OF EQUIVALENT VORTEX= 1.41
CORRECTION ACCURACY= 94.3 PERCENT
ACCURACY IN TOTAL CL= 1.0 PERCENT

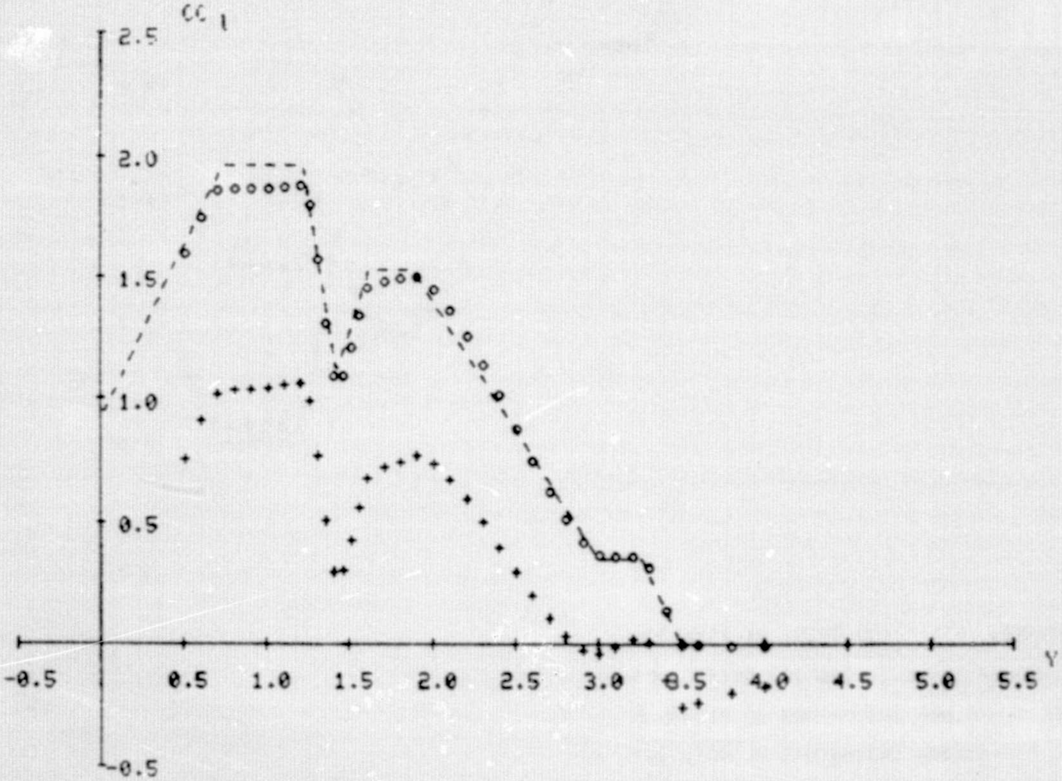

Figure D-14

ENTER RUN NUMBER: 23
TRAVERSE DISTANCE= 1.50 CHORDS
TOTAL WING LIFT COEFFICIENT= 1.19
LOCATION OF EQUIVALENT VORTEX= 2.86
STRENGTH OF EQUIVALENT VORTEX= 1.39
CORRECTION ACCURACY= 94.9 PERCENT
ACCURACY IN TOTAL CL= 1.0 PERCENT

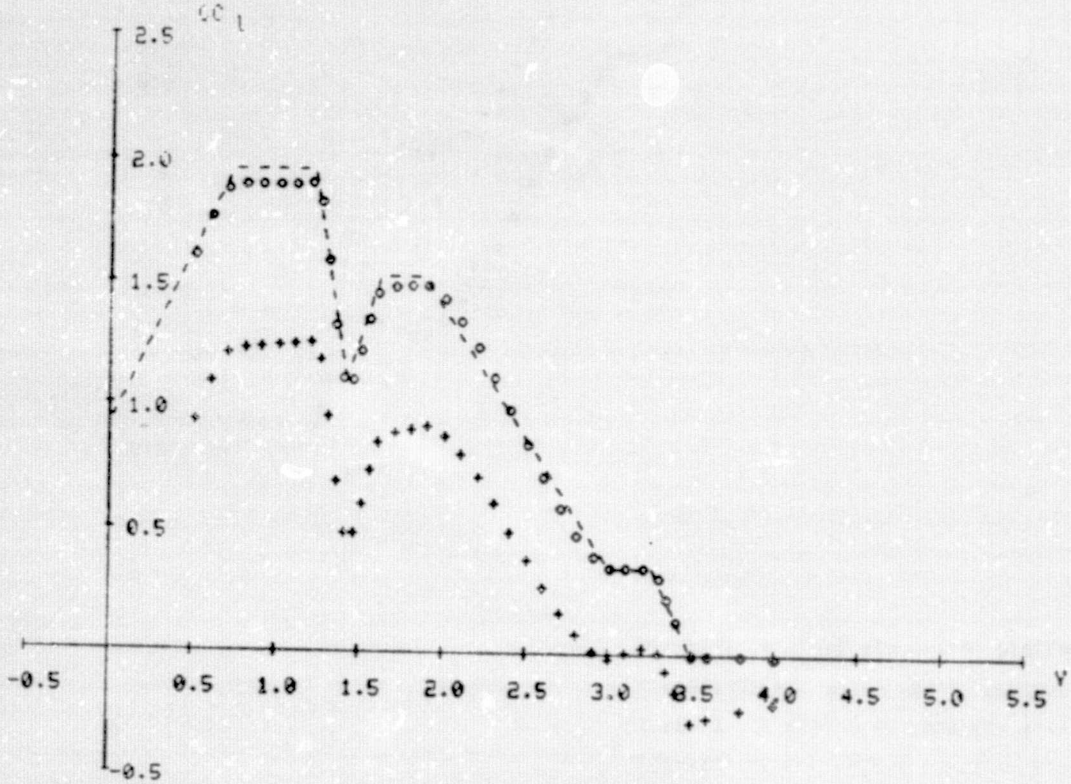

Figure D-15

ENTER RUN NUMBER: 24
TRAVERSE DISTANCE= 2.00 CHORDS

TOTAL WING LIFT COEFFICIENT= 1.19

LOCATION OF EQUIVALENT VORTEX= 2.92

STRENGTH OF EQUIVALENT VORTEX= 1.36

CORRECTION ACCURACY= 95.4 PERCENT

ACCURACY IN TOTAL CL= 1.0 PERCENT

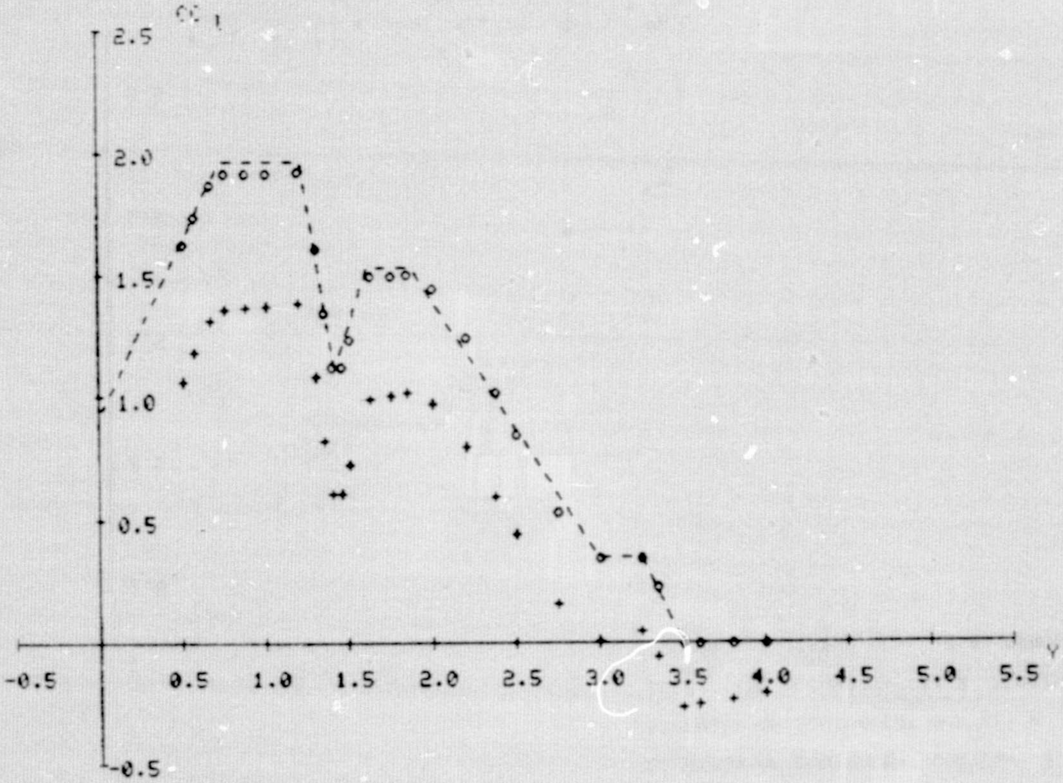

Figure D-16

ENTER RUN NUMBER: 12
TRAVERSE DISTANCE= 0.25 CHORDS

TOTAL WING LIFT COEFFICIENT= 1.86

LOCATION OF EQUIVALENT VORTEX= 2.70

STRENGTH OF EQUIVALENT VORTEX= 2.17

CORRECTION ACCURACY= 84.2 PERCENT

ACCURACY IN TOTAL CL= 2.0 PERCENT

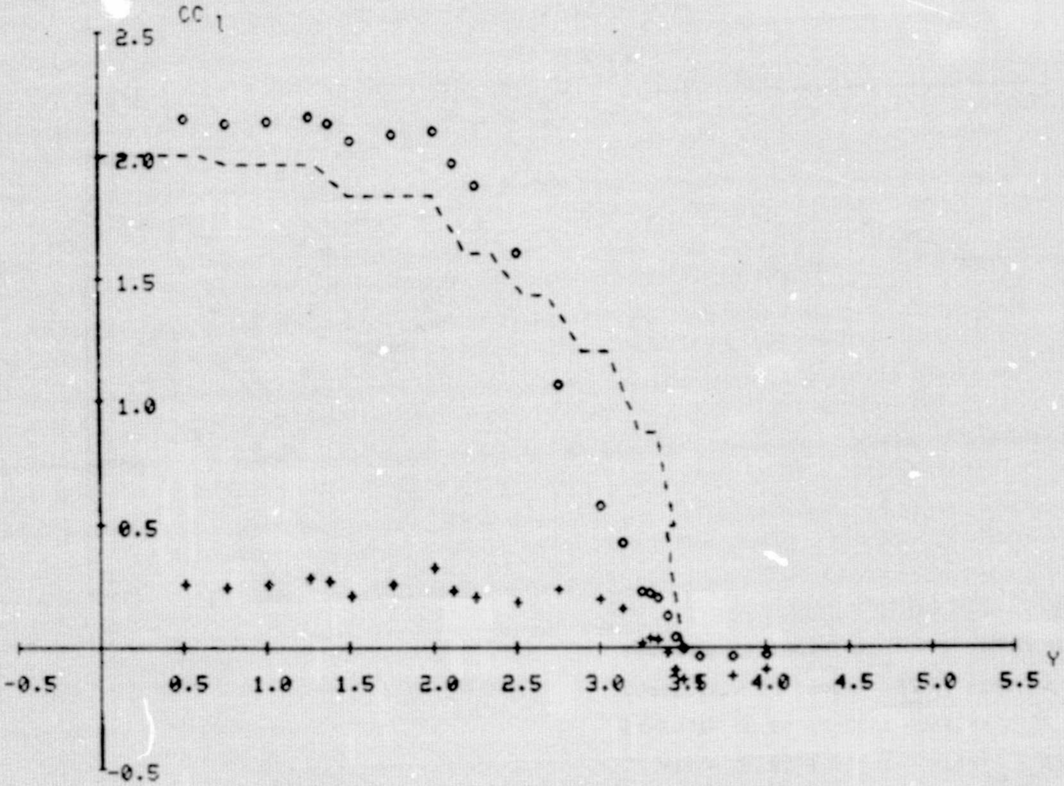

Figure D-17

ENTER RUN NUMBER: 14
TRAVERSE DISTANCE= 0.35 CHORDS
TOTAL WING LIFT COEFFICIENT= 1.66
LOCATION OF EQUIVALENT VORTEX= 3.02
STRENGTH OF EQUIVALENT VORTEX= 1.95
CORRECTION ACCURACY= 94.4 PERCENT
ACCURACY IN TOTAL CL= 1.0 PERCENT

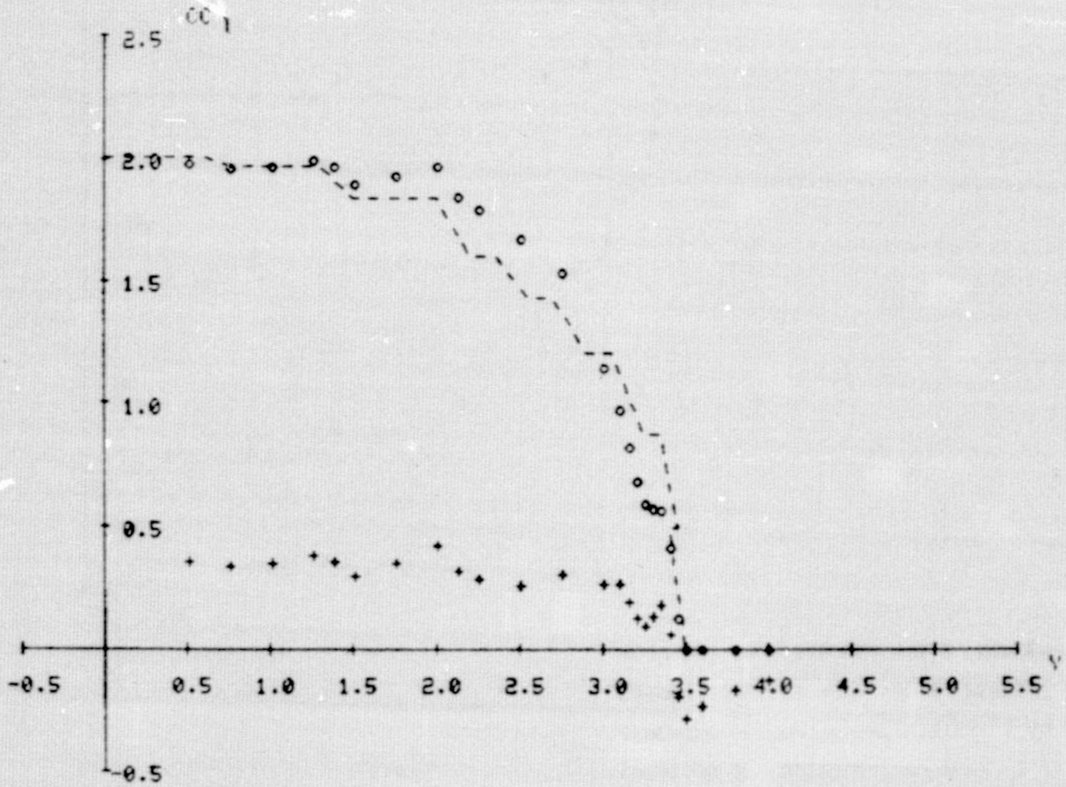

Figure D-18

ENTER RUN NUMBER: 11
TRAVERSE DISTANCE= 0.50 CHORDS

TOTAL WING LIFT COEFFICIENT= 1.66

LOCATION OF EQUIVALENT VORTEX= 3.14

STRENGTH OF EQUIVALENT VORTEX= 1.89

CORRECTION ACCURACY= 95.8 PERCENT

ACCURACY IN TOTAL CL= 1.0 PERCENT

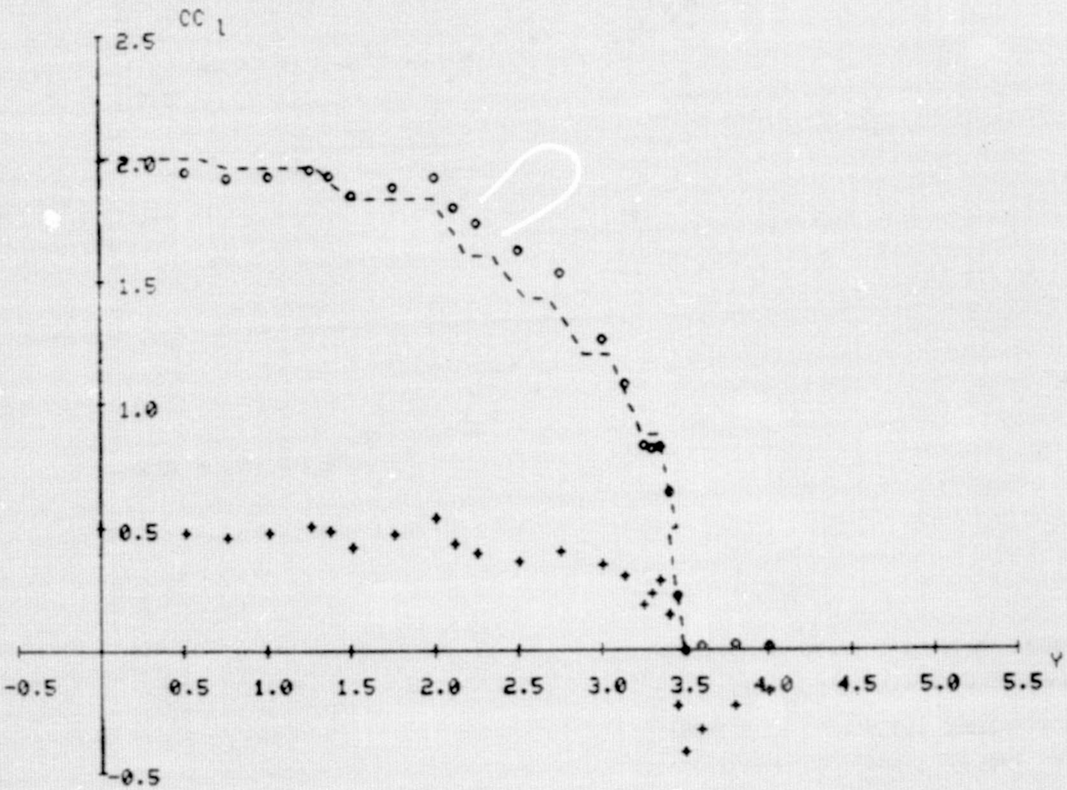

Figure D-19

ENTER RUN NUMBER: 10
TRAVERSE DISTANCE= 1.00 CHORDS

TOTAL WING LIFT COEFFICIENT= 1.66

LOCATION OF EQUIVALENT VORTEX= 3.07

STRENGTH OF EQUIVALENT VORTEX= 1.95

CORRECTION ACCURACY= 97.9 PERCENT

ACCURACY IN TOTAL CL= 1.0 PERCENT

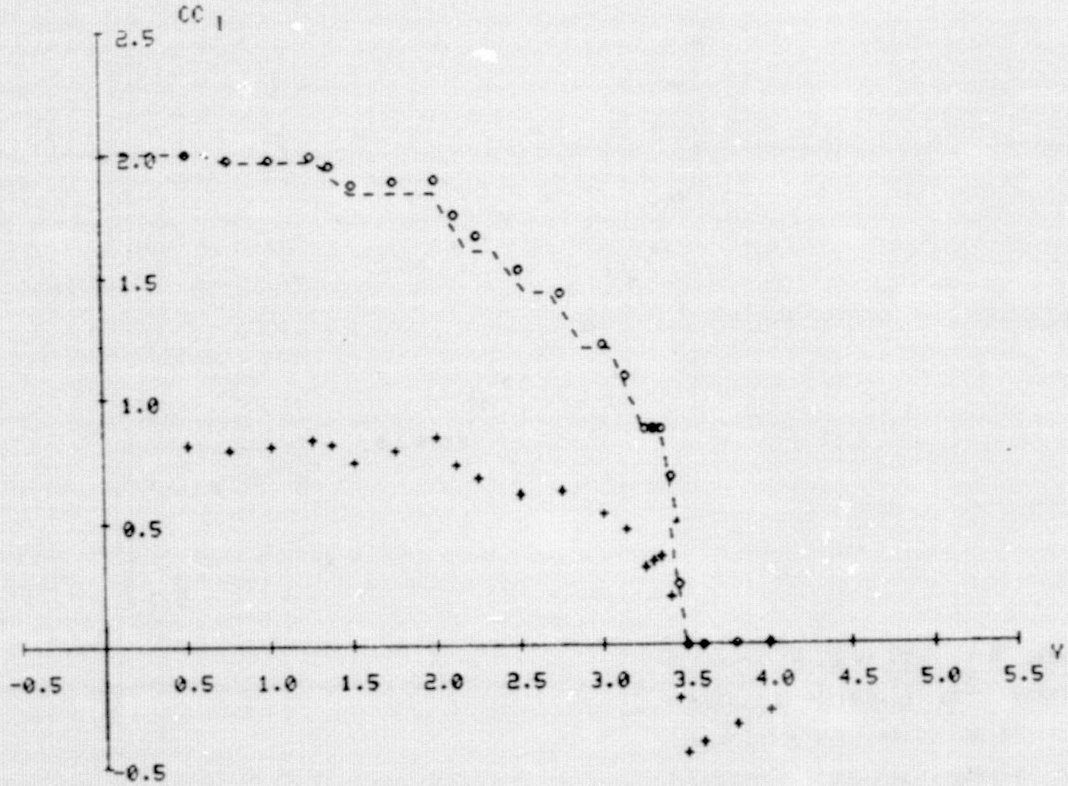

Figure D-20

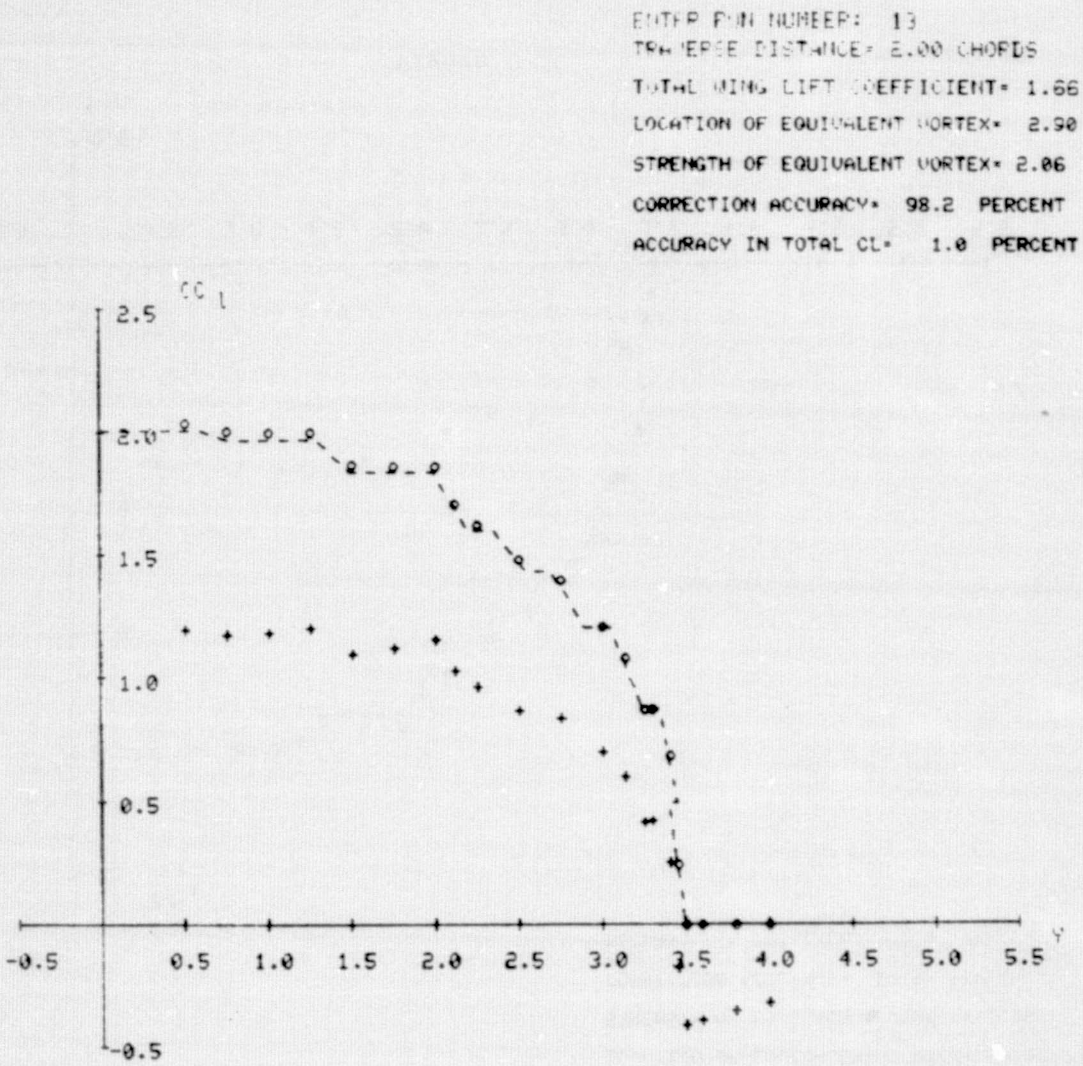
ENTER RUN NUMBER: 13
TRAVERSE DISTANCE= 2.00 CHORDS
TOTAL WING LIFT COEFFICIENT= 1.66
LOCATION OF EQUIVALENT VORTEX= 2.90
STRENGTH OF EQUIVALENT VORTEX= 2.06
CORRECTION ACCURACY= 98.2 PERCENT
ACCURACY IN TOTAL CL= 1.0 PERCENT
CC L
2.5
2.0
1.5
1.0
0.5
-0.5
-0.5
0.5
1.0
1.5
2.0
2.5
3.0
3.5
4.0
4.5
5.0
5.5
Y

Figure D-21

1. Report No.	2. Government Accession No.	3. Recipient's Catalog No.
NASA TM-73,247		

4. Title and Subtitle	5. Report Date
DETERMINING THE LIFT AND DRAG DISTRIBUTIONS ON A THREE-DIMENSIONAL AIRFOIL FROM FLOW-FIELD VELOCITY SURVEYS	6. Performing Organization Code
7. Author(s): Kenneth L. Orloff	8. Performing Organization Report No.: A-7062
9. Performing Organization Name and Address: Ames Research Center, Moffett Field, Calif. 94035	10. Work Unit No.: 505-10-12
	11. Contract or Grant No.
12. Sponsoring Agency Name and Address: National Aeronautics and Space Administration, Washington, D.C. 20546	13. Type of Report and Period Covered: Technical Memorandum
	14. Sponsoring Agency Code

15. Supplementary Notes

16. Abstract

The application of the incompressible momentum integral equation to a three-dimensional airfoil is reviewed. The objective is to interpret the resulting equations in a way that suggests a reasonable experimental technique for determining the spanwise distributions of lift and drag. Consideration is given to constraints that must be placed on the character of the vortex wake structure shed by the wing, to provide the familiar relationship between lift and bound vorticity. It is shown that the induced drag distribution is not directly measurable, but can be obtained, via the lift distribution, approximately for a deflected wake and exactly for a planar wake. A novel technique is presented for obtaining the spanwise lift distribution from velocity surveys behind the wing. Moreover, it is shown that it is only necessary to survey a short distance above and below the wing trailing edge. While the measured lift coefficient is not the true value, it is, nevertheless, accurate. The necessary formalism is developed to correct these measured values by using an equivalent single vortex model to account for the unmeasured portion of the downward (or upward) momentum. Examples are presented for several typical loading distributions and the results of a numerical simulation of the suggested experiment are discussed.

17. Key Words (Suggested by Author(s))	18. Distribution Statement
Aerodynamics Wind-tunnel testing Flow velocity measurements	Unlimited STAR Category - 02

19. Security Classif. (of this report)	20. Security Classif. (of this page)	21. No. of Pages	22. Price*
Unclassified	Unclassified	76	$4.75

*For sale by the National Technical Information Service, Springfield, Virginia 22161